# Friction-induced artifact in atomic force microscopy topographic images

Thales Fernando Damasceno Fernandes

Belo Horizonte

2014

# Friction-induced artifact in atomic force microscopy topographic images

Thales Fernando Damasceno Fernandes

Orientador: Prof. Bernardo Ruegger Almeida Neves

Dissertação apresentada à UNIVERSIDADE FEDERAL
DE MINAS GERAIS, como requisito parcial para a
obtenção do grau de MESTRE EM FÍSICA.

Belo Horizonte
2014

*“Somewhere, something incredible*
*is waiting to be known.”*
*Carl Sagan*

## Acknowledgments

À Karina, por ter me incentivado a ingressar na iniciação científica e assim dar início a essa nova formação e uma mudança de vida bastante promissora. Por sempre estar ao meu lado me apoiando, dando sentido e propósito a minha vida.

Ao professor Bernardo, pela oportunidade a mim dada, me orientando e aconselhando sempre que preciso e por ter me mostrado essa nova área da ciência.

Aos meus pais, por terem me embarcado nessa formação acadêmica de qualidade.

À todo o pessoal do Labnano, por sempre estarem dispostos a ajudar.

À UFMG pela infraestrutura.

À CNQP, CAPES e FAPEMIG pelo financiamento.

## Table of contents

Acknowledgments ........ iii

Table of contents ........ iv

Abstract ........ vi

Resumo ........ vii

Introduction ........ 1

Chapter 1 – Atomic Force Microscopy ........ 3

1.1 – Microscope Setup ........ 3

1.2 – Photodetector ........ 4

1.3 – Scan Direction ........ 5

1.4 – Lateral Force Microscopy ........ 8

1.5 – Force Curve ........ 9

Chapter 2 – Topographic Artifact ........ 12

2.1 – Qualitative Understanding ........ 12

2.2 – Experimental Results ........ 14

2.3 – Analytical Theory ........ 18

2.3.1 – Euler-Bernoulli Beam Theory ........ 18

2.3.2 – Constant Deflection ........ 23

2.3.3 – Topography Artifact ........ 25

2.4 – Numerical Results ........ 27

2.4.1 – Finite element method .......... 27

2.4.2 – Cantilever Model .......... 28

2.4.3 – 3D Simulation .......... 30

2.4.4 – Constant Deflection (2D) .......... 36

Conclusions .......... 39

References .......... 41

Appendix A – Infinitesimal strain .......... 47

Appendix B – Anisotropic cantilever .......... 49

Appendix C – Compression of a cantilever .......... 51

## Abstract

In Contact Mode Atomic Force Microscopy (CM-AFM), a cantilever with a sharp tip on its end is employed to acquire topographic information. Such acquisition is normally made by monitoring the deflection of the cantilever when it is in contact with the surface being scanned and using deflection variations as a feedback signal to the control electronics in order to keep the deflection constant (also known as constant force imaging mode in the literature). However, there is a major problem with this approach since, in most cases, a constant force scanning is not possible: frictional forces, besides normal forces, may bend the cantilever. Such additional bending (deflection) needs to be considered in the formulation of the problem. The present dissertation investigates how these forces (frictional and normal) can give rise to a topographic artifact when scanning along the cantilever axis direction. Such artifact is even more dramatic when the friction coefficient of the sample changes from region to region.

This effect is studied experimentally, with a sample composed of graphene monolayer atop silicon oxide. The observed artifact, caused by frictional forces, causes the graphene to appear either thicker or thinner than it really is depending on scan direction. A theoretical examination is also made both with analytical methods (Euler-Bernoulli beam theory) and a simulation on COMSOL Multiphysics package. The theory not only predicts the artifact, but also indicates how it can be completely avoided by changing the scanning angle to the perpendicular direction of the cantilever axis.

# Resumo

No Modo Contato da Microscopia de Força Atômica (CM-AFM), uma alavanca com uma ponta bastante afiada em sua extremidade é usada para adquirir informação topográfica. Tal aquisição normalmente é feita monitorando a deflexão da alavanca quando em contato com a superfície a ser varrida. Usa-se a variação da deflexão como um sinal de *feedback* que controla a eletrônica, mantendo a deflexão constante (conhecido como modo de força constante na literatura). Porém, existe um grande problema com essa abordagem, já que, na maioria dos casos, fazer uma varredura com força constante não é possível: forças de atrito, além da força normal, podem fletir a alavanca. Tal curvatura adicional (deflexão) deve ser considerada na formulação do problema. Essa dissertação investiga como essas forças (normal e de atrito) podem dar origem a um artefato de topografia quando é feito uma varredura ao longo do eixo da alavanca. Tal artefato é ainda mais dramático quando o coeficiente de atrito da amostra muda de região para região.

Esse efeito é estudado experimentalmente, com uma amostra composta de uma monocamada de grafeno em cima de oxido de silício. O artefato observado, causado pelas forças de atrito, faz o grafeno aparecer mais espesso ou mais estreito do que realmente é, dependendo da direção de varredura. Uma verificação teórica também é feita usando métodos analíticos (teoria de vigas de Euler-Bernoulli) e simulações usando o pacote *COMSOL Multiplysics*. A teoria não apenas prediz o artefato, mas também indica como ele pode ser completamente evitado ao trocar o ângulo de varredura para perpendicular à direção do eixo da alavanca.

# Introduction

Atomic Force Microscopy (AFM) is a technique capable of imaging surfaces with atomic resolution [1–10]. It works by employing a sharp tip ($\sim 10nm$ of diameter at the apex) mounted on a cantilever a few hundred micrometers long. When the tip is approached to the surface being scanned, the surface-tip interaction forces deform the cantilever, causing a deflection (bending) of the cantilever. Monitoring the deflection of the cantilever by means of optical reflection and computer electronics (controller $+$ computer), when the tip is in contact with the surface, enables the acquisition of topographic information of the surface with atomic resolution. This type of operation, when the tip is in contact with the sample, is called Contact Mode (CM) [4–6]. Another type of operation is the Non-Contact Mode (NCM) [1,2,4,5,9], where the tip is oscillated above the sample and, by measuring the amplitude or frequency shift of the cantilever when the tip is in the proximities of the sample, a topographic profile is also created. In this Dissertation, only the Contact Mode Atomic Force Microscopy (CM-AFM) will be addressed.

In CM-AFM, what is monitored by means of the computer electronics is the cantilever deflection, which is called setpoint. Since the cantilever works similarly to a spring, there is a direct relationship between the deflection (setpoint) and the normal force, the force between the tip and the surface. Therefore, it is always possible to convert deflection to force using Hooke's Law. The system electronics will try to keep the cantilever deflection constant, by raising or lowering the sample as its topography changes, thus operating in a constant deflection mode, which is usually called in AFM as constant force mode.

In the description of the operation of the AFM in contact mode, generally only the normal force enters on the analysis of the problem. This might be a major issue, since frictional forces can cause substantial deflection of the cantilever, and since this force is unaccounted in the theory of CM-AFM, unexpected results might be produced. As a consequence of such frictional forces, in regions with higher frictional coefficients, the cantilever will bend more or less, depending on the scan direction. Since this frictional force was unaccounted, the electronics will perceive this change in deflection as a change in normal force (even if the normal force did not change), and since the microscope is operated in a constant deflection mode, the electronics will move the tip to compensate these frictional

forces. In summary, what these frictional forces do is the following: sample regions with high frictional coefficient appear higher or lower than they really are depending on the scan direction. Consequently, they modify the topographic information and introduce a topographic artifact. Although this artifact is normally in the nanometer range, this might be a major problem when investigating ultrathin samples. For example, in recent years, with the discover of graphene [11,12] and other two dimensional materials like hexagonal boron nitride [13–19], molybdenum disulfide [20–22] and others [23–25], it became important to measure small structures with sub-nanometer precision. If there is an artifact in nanometer range, the measurements become unreliable.

In this Dissertation, this topographic artifact was investigated by means of both an analytical theory and finite elements simulation [26–32], using Comsol Multiphysics. It will also be seen that experimental results agree well with the predicted analytical formulae for the topographic artifact and that it is possible to eliminate this artifact by choosing another scanning direction, perpendicular to the cantilever. In this geometry, there is no artifact. And as such, we propose it as a standard for CM-AFM measurements. Regardless of the force being employed and of the type of surface being scanned, it is preferable to make all measurements in this perpendicular-to-the-cantilever geometry and, as an additional bonus, Lateral Force [1–4,9] (LF-AFM) signal is also simultaneously acquired.

# Chapter 1 – Atomic Force Microscopy

This chapter describes in more details the working principles of an AFM and how its theory is usually treated in the literature.

## 1.1 – Microscope Setup

The basic principles of the AFM are very simple. In Fig 1, there is a basic scheme of a typical AFM microscope. The sample is mounted on top of a piezoelectric tube (the scanner), capable of moving the sample in 3 orthogonal axes. The cantilever is mounted in the proximities of the sample being scanned. The laser and the photodetector that measures the cantilever deflection are also shown in Fig 1. Finally, the system electronics, that consists of a controller for the microscope hooked up on a computer that controls the controller and displays images.

The actual process of image acquisition and operation is as follows: when the cantilever starts to approach the sample, it starts to feel the interaction forces [2,5,10] between the atoms of the tip and the surface. These forces are, typically, Van der Waals forces [33,34]. The laser hits the back of the cantilever, which is reflective, and the reflected light is bounced on the 4-quadrant photodetector (Fig 2). Deflection of the cantilever is translated into a vertical difference signal on the photodetector. Thus, this detector is a very sensitive angle measurement device[1], capable of measuring very small deflections (angles) of the cantilever, in the typical range of millidegrees. The signal of the photodetector is monitored by the system electronics. In Contact Mode Atomic Force Microscopy (CM-AFM), the deflection of the cantilever should be constant (setpoint). For this, the electronics will try to make the signal on the detector constant, equal to the setpoint, by lowering or raising the sample by means of the piezoelectric tube. This change in height is captured by the computer and is translated into an image, which has the topographic profile of the surface.

[1] Changes in the cantilever deflections changes the laser path, this will change the laser position on the photodetector. So changes in laser positions are correlated with changes in the laser path, with are essentially changes in angle of incidence.

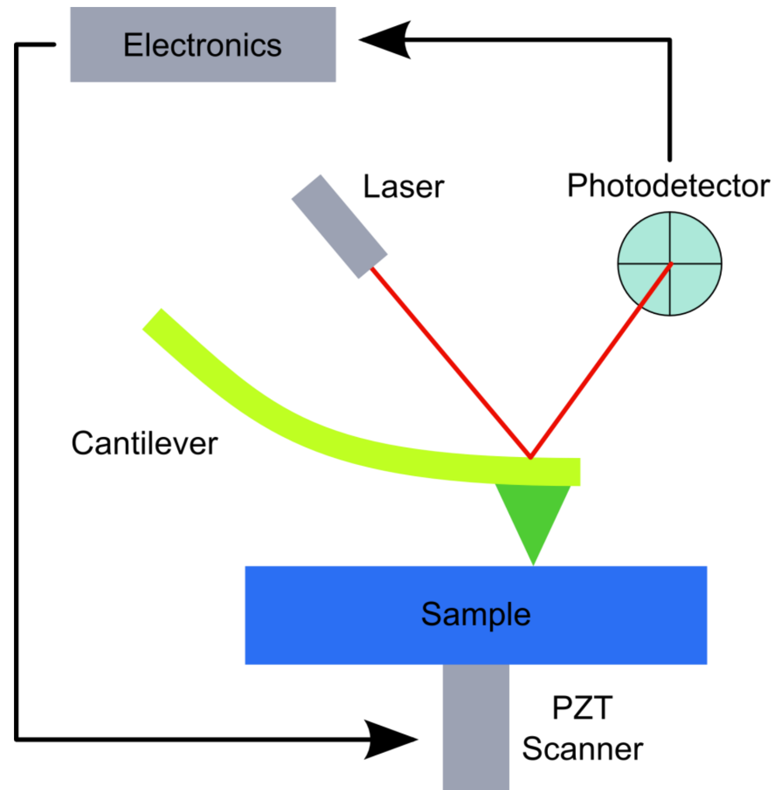


***Fig 1**. Scheme of a typical Atomic Force Microscope.*

## 1.2 – Photodetector

As cited above, the photodetector usually has 4 quadrants as in Fig 2. The top 2 quadrants are called $A$ while the bottom two are called $B$, the left two are called $C$ while the right two are $D$. The way the photodetector measures signal is as follows: The laser spot is projected onto the photodetector, but its spot size is not punctual as represented here; it usually covers all the 4 quadrants. The laser will be more incident on some quadrants than others. So the signal of $A - B$, the voltage difference between $A$ and $B$, will give how much the laser is displaced in the vertical direction of the detector. The same applies to $C - D$ and it will indicate how much the laser is displaced in the horizontal direction. Therefore, the photodetector is a differential signal detector; it gives the difference in signal between the regions of the detector, thus providing the "location" of the laser, the region with greater intensity. This signal up-down or left-right is directly proportional to the deflection (angle) of the cantilever. Bending of the cantilever causes increase/decrease of the $A - B$ signal, while torsion of the cantilever causes increase/decrease of the $C - D$ signal as in Fig 3.

When operating the microscope in the CM-AFM mode, the $A - B$ signal is the only one of importance, since this is the signal used in the feedback loop and it is this signal that is maintained constant by means of the setpoint. The $C - D$ signal plays no role in the feedback loop and it is only used to acquire the Lateral Force signal [3,6,9].

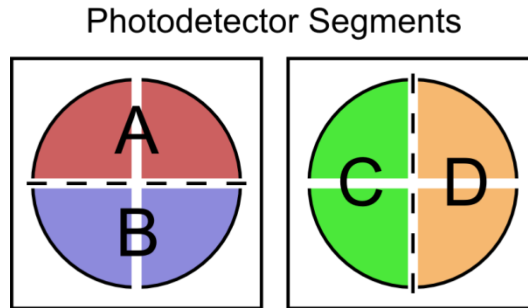


*Fig 2. How the four quadrants of a photodetector are divided. The differential signal $\boldsymbol{A - B}$ tell us the vertical position of the laser, while the signal $\boldsymbol{C - D}$ tell us the horizontal position.*

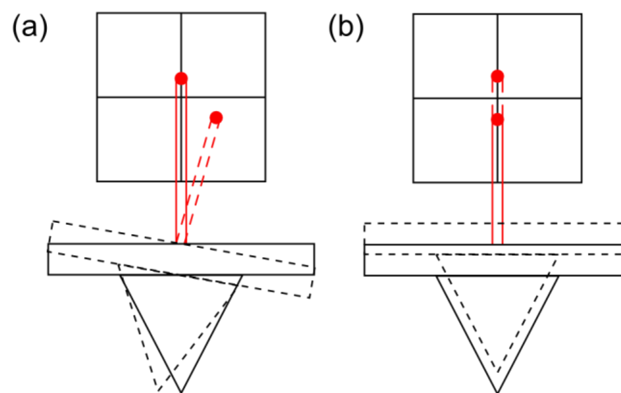


*Fig 3. How deflections of the cantilever get translated into signal. In (**a**), twists (torsions) in the cantilever cause the laser to go to the left or to the right. In (**b**), bending along the cantilever beam causes the laser to go up and down.*

## 1.3 – Scan Direction

Fig 4 shows a scheme of the AFM image acquisition. Here are defined two axes, a slow-scan axis and a fast-scan axis. The tip of the cantilever travels in the fast-scan axis back and forth acquiring a line of an AFM image. After moving back and forth on the fast-scan axis the scanner moves upwards a little (in the slow-scan axis) to acquire a new line and the cycle continues. In this way the fast-scan axis are responsible for the lines of the image, while the slow-scan is responsible for acquisition of multiples lines in the image.

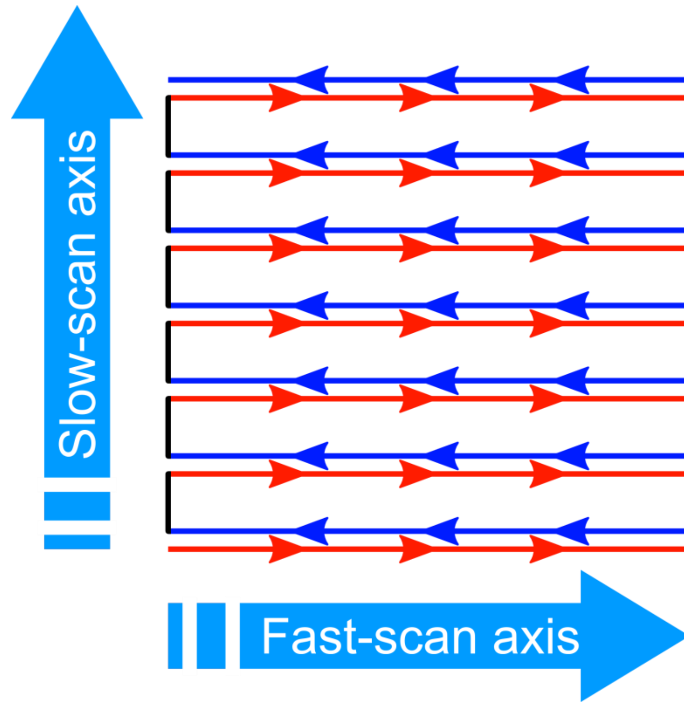


***Fig 4***. *The definition of the fast-scan and slow-scan axis. The scanner moves back and forth on the fast-scan axis, acquiring a line of an AFM image, while moving slowly in the slow-scan axis to acquire more lines.*

Fig 5 shows a scheme of the microscope top view. Two directions are defined: parallel or perpendicular to the cantilever. It is also possible to scan in any other direction, forming an angle with these, but they are unimportant and, here, only those two will be compared, since other directions are linear combinations of these two. These directions are defined as the scanner fast-scan axis; so, in a parallel direction the fast-scan axis is in the direction parallel to the cantilever axis (the cantilever moves in the left to right direction), while in the perpendicular direction, the cantilever moves in the top to bottom direction, according to the geometry shown on Fig 5. So while scanning, in whatever direction, there will always be two images (represented as the blue and red arrows in Fig 4). These scan directions are called trace (Fig 4 red arrow) and retrace (Fig 4 blue arrow), also called forward and backward direction images, respectively. These two directions are acquired simultaneously[2] in two channels by the microscope.

---

[2] The microscope works in this back and forth manner, scanning from left to right and then right to left, one scan channel is acquired in the travel from left to right and the other channel is acquired in right to left travel. The two channels are acquired sequentially in this manner, alternating between single lines acquisition. So the blue arrow in Fig 4 is responsible for one channel while the red arrow is the image for the other channel.

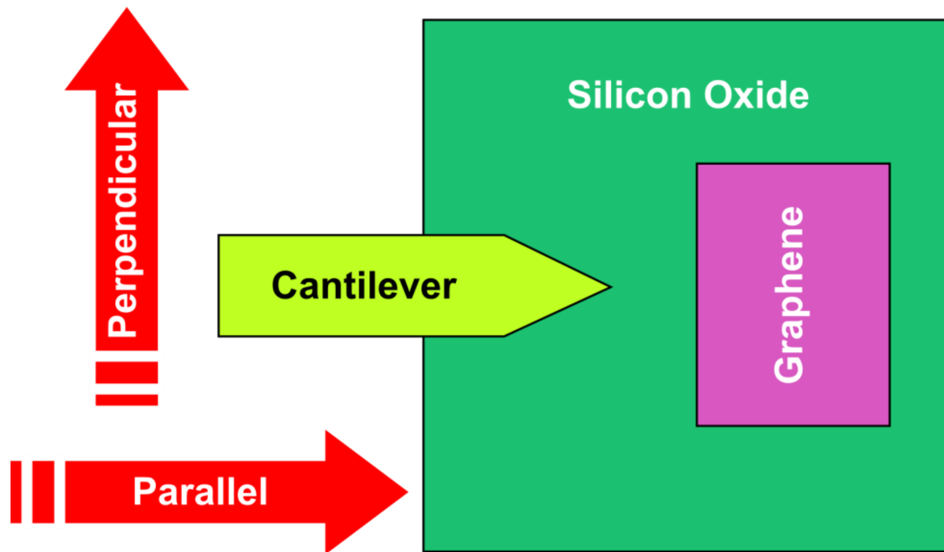


***Fig 5****. The definition of the Parallel and Perpendicular scan directions. Parallel being along the axis of the cantilever, and perpendicular being perpendicular to the axis. This figure also shows the top view of the experimental setup.*

There is a clear symmetry in the forward/backward direction of the perpendicular direction (mirror symmetry on the $x$ axis, the axis along the cantilever), while there is an asymmetry in the parallel direction. In the forward direction in the perpendicular geometry the cantilever moves from top to bottom, if we use a mirror in the $x$ axis, this scan will be transformed to a bottom to top scan, still in a perpendicular geometry, so there is a symmetry in this geometry; in the perpendicular scan, there is no symmetry, no mirror at all can transform a forward scan to a backward scan, so they are asymmetric. The symmetry in the perpendicular direction can be thought as a more similar signal in the forward/backward channels; in the parallel direction there is an asymmetry in the geometry, this can be an indicator that the signal will be dissimilar, and it is further explored in a qualitative argument in section 2.1 – Qualitative Understanding.

Normally, it is a matter of choice, or taste, to choose between these two directions (perpendicular and parallel) for the fast-scan axis, or as a matter of fact, any angle at all. What is usually done is to opt for the default direction of the specific microscope; some have perpendicular as a default direction, while others have parallel. Some microscopes also have the default feature of showing both channels (forward and backward), while others usually only show a single channel. It is usually a good choice to choose the default configuration of the microscope, since it usually gives more stable and precise measurements, since this direction is used more often. But it is not a good idea to choose blindly any direction without

further reason to do so, for the commodity of being default. As a good practice, it is always wise to see both channels (forward and backward) and compare them; if they yield equal results, then it is likely that the topography is being properly imaged.

A quote from B. Bhushan [10], *"Topographic measurements are made at any scanning angle. At a first instance, scanning angle may not appear to be an important parameter. However, the friction force between the tip and the sample will affect the topographic measurements in a parallel scan (scanning along the long axis of the cantilever). Therefore a perpendicular scan may be more desirable. Generally, one picks a scanning angle which gives the same topographic data in both directions; this angle may be slightly different than that for the perpendicular scan."*.

While it is fairly well known that friction can alter topographic information on parallel scan, it is not well understood how friction influences the topography and by how much in the parallel scan direction. What is usually done is; if there is any mismatch between forward and backward images, simply choose another scanning angle that gives no mismatch. Also, there is no consensus or even a standard of which direction should be used in the literature, or even worst, any guidelines to always acquire both channels. Notwithstanding, in the literature, it is known that, in a parallel scan, the measurements can suffer from artifact, this geometry is still in use, even with the shortcoming of not acquiring Lateral Force measurements simultaneously.

## 1.4 – Lateral Force Microscopy

Lateral Force Microscopy (LFM) [3,6,9] is a technique of the family of techniques of Scanning Probe Microscopy (SPM) [2,4–6,8–10] that acquires information on frictional forces. It can be acquired simultaneously with the signal of CM-AFM. For it to work properly, the scan direction needs to be on the perpendicular geometry, since the cantilever needs to twist as explained below. While the tip scans the surface, regions with different frictional coefficients will give rise to frictional forces with different magnitudes. High frictional coefficient regions will deform (rotate, twist) more the cantilever than low frictional coefficient regions. This can be seen in Fig 6: when the tip passes a region with different frictional coefficient, it will be more twisted and will deform more, thus augmenting the $C - D$ signal on the photodetector. This signal $C - D$ is translated as a LFM image that can be

interpreted in a quantitative way to determine the frictional coefficient of the surface. The only problem with this technique is the determination of the torsional spring constant, the constant that translates rotation of the cantilever to force by means of Hooke's Law (for twist). Its determination is not as simple as the bending spring constant, where several methods, as thermal tuning [35–42], Sader Method [36,39,42], or others [37–39,41,42] can be used. In order to determine the torsional spring constant, it can be used the Sader Method for torsion [42], or other methods [43–49].

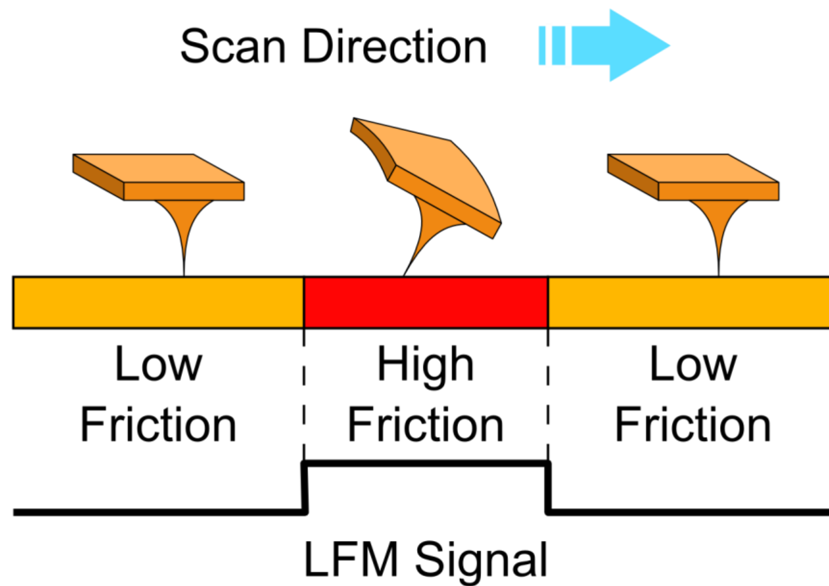


***Fig 6***. *The basic operation of LF-AFM. Regions with high friction will twist the cantilever, rotating it. While regions with very low friction will not deform the cantilever significantly.*

## 1.5 – Force Curve

The photodetector signal (deflection) is normally in Volts. Therefore, a way to translate this signal in Volts to a signal in Newtons is needed and this is done by means of a Force Curve. In this way, it is possible to know the interaction forces between the tip and the sample surface.

In Fig 7 shows a typical force curve. The cantilever is lowered (red curve) onto the sample and then raised (blue curve). In $\boldsymbol{A}$, the cantilever is lowered from a large distance from the sample; in $\boldsymbol{B}$ it starts to feel the interaction forces between the system cantilever-sample and suddenly jumps into contact, (snap-in); in $\boldsymbol{C}$, the cantilever is in hard contact with the sample and the forces onto the cantilever are repulsive, so it starts to deform; in $\boldsymbol{D}$ the

cantilever is being attracted by the sample while distancing from it, this attractive force may be dominated by the contamination layer that it is present in air [1,2,5,7–9] and forms a water meniscus (see Fig 8), this force is typically a capillary force; in ***E*** the attractive forces are not enough to bend the cantilever any further and the contamination layer ceases to have a meniscus and it breaks, suddenly jumping out of contact with the surface (snap out). It, then, retreats to ***F*** to start the cycle over if desired.

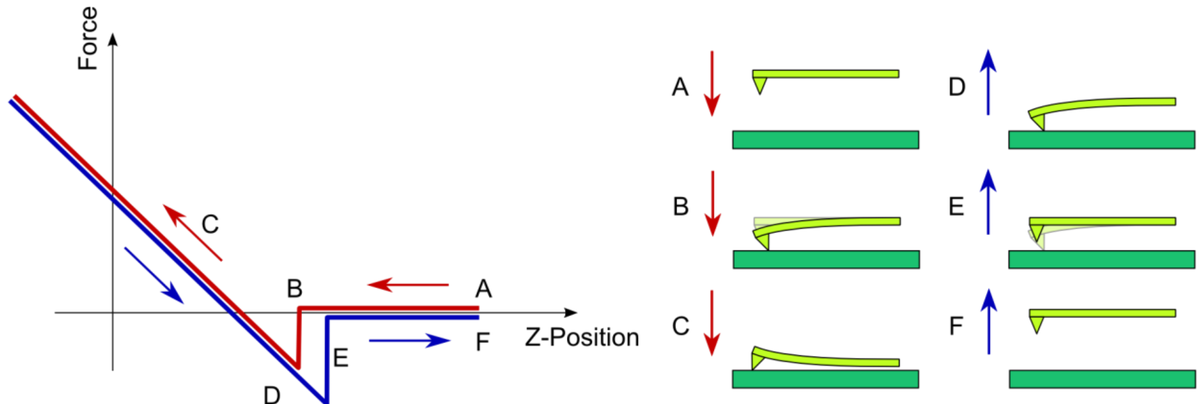


***Fig 7***. *A typical force curve. In red it shows the cantilever being lowered and in blue it being raised.*

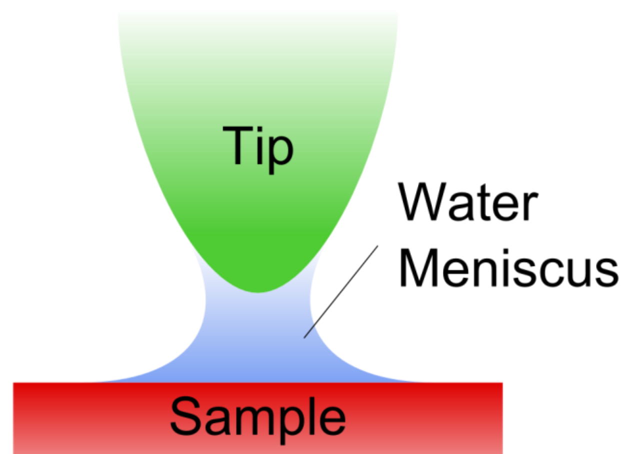


***Fig 8***. *Water meniscus. When the tip it is near the sample, the contamination layer (mostly water) forms a meniscus. This meniscus is the principal reason for the adhesion forces in a standard Force Curve.*

The inclination of this curve (Fig 7) is called in the sensibility. Since the signal of the photodetector ($y$ axis) is in Volts, and the travel distance of the cantilever, Z-Position, ($x$ axis) is in nanometers, the sensibility is expressed as the ratio of the two: Volts per nanometer. Since the cantilever behaves as a spring [50–56] (its behavior with low deflection is linear), it is possible to use Hooke's Law as $\mathbf{F} = -k\Delta\mathbf{x}$. Using the sensibility and Hooke's Law, it is

possible to express the force on the cantilever in function of the setpoint (in Volts) as $|F| = Sk\Delta V$, where $\Delta V$ is the setpoint, it follows from $\Delta x = S\Delta V$. With these formulas, it is possible to convert a reading in the photodetector ($A - B$ signal) to a force on the cantilever.

However, there is a major problem with this conventional CM-AFM approach since, in most cases, a constant deflection scanning is not possible: frictional forces, besides normal forces, may bend the cantilever. Such additional bending (deflection) needs to be considered in the formulation of the problem. The present work investigates how these forces (friction and normal) can give rise to a topographic artifact when scanning along the cantilever axis direction.

Since now there are two forces on the cantilever tip, a normal force and a frictional force, it is not possible to uniquely determine the force on the cantilever solely on its deflection, since its deflection is partially caused by the normal force and the other part by the frictional forces.

The frictional forces can be decomposed into two forces, one proportional to the normal (Amonton’s Law) and another due to capillary forces (also called adhesion force), that arises from the water meniscus. This adhesion force is highly dependent on temperature, humidity, sample-probe distances, and others factors.

# Chapter 2 – Topographic Artifact

This chapter investigates, in depth, how to model the Contact Mode in AFM to account for frictional forces and how these forces may affect topography measurements. An analytical theory is developed based on structural mechanics and a finite elements simulation on COMSOL Multiphysics 4.4 is also carried out. At the end of this chapter, some guidelines on how to do CM-AFM avoiding artifacts are proposed.

## 2.1 – Qualitative Understanding

By making a Force Curve (section 1.5 – Force Curve) and, therefore, determining the sensibility of the system cantilever-microscope[3], it is possible to link a force with a deflection with the knowledge of the spring constant. This is a one to one map, since it is a quasi-static situation. The cantilever is static and is in a concave deflection as shown in Fig 9a.

In Fig 9b, the cantilever is moving in the backward direction (moving to the left), therefore the frictional forces on the tip will be to the right; this force will bend the cantilever more, leaving it with a more concave deflection. In the forward direction, Fig 9c (moving to the right), the frictional forces will be to the left, and this force will try to unbend the cantilever, leaving it in a less concave deflection. Here, for the sake of illustration, it is shown the deflection as convex, but, in reality, it would still be concave, but less than in Fig 9b.

[3] This sensibility may change if measurements were made in different days, since the sensibility is highly correlated to the laser and its location on the back of the cantilever. Changes in the spring constant, if any, are insignificant and in the range of the expected error of the measuring instruments.

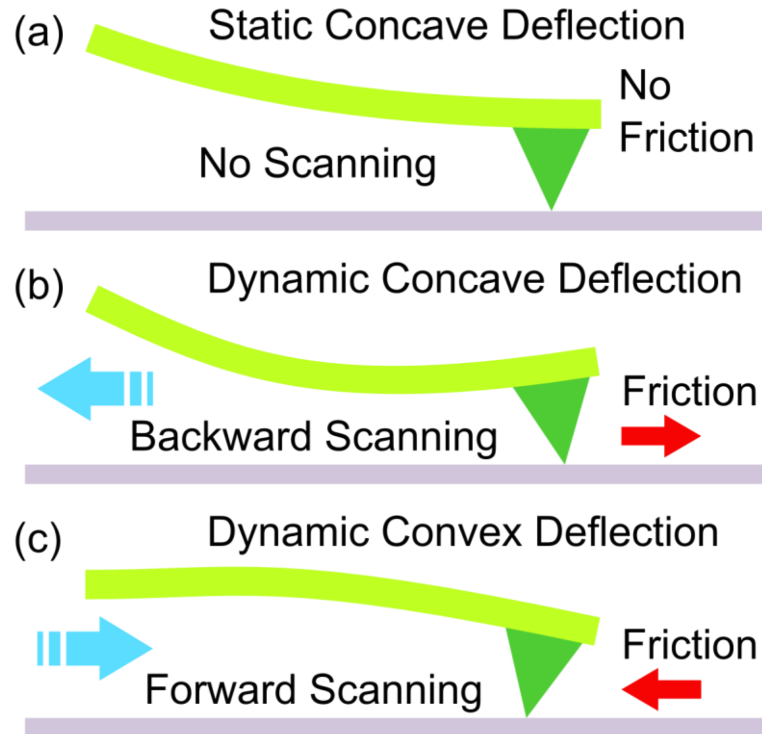


***Fig 9***. *Qualitative picture of the topographic artifact. In (**a**), the cantilever is lowered to the surface while in a static situation (no scanning). Figure (**b**) shows a scan in the backward direction (to the left), so friction is in the opposite direction (to the right). Figure (**c**) shows a scan in the forward direction (to the right), so friction is to the left. In (**b**) the cantilever is more bent than in (**a**), while in (**c**) it is less bent than in (**a**).*

In all 3 cases (Fig 9a-c), it is assumed the normal force to be equal and only the friction changes. As stated before, CM-AFM is a technique of constant deflection: the setpoint specifies a deflection (a reading in the photodetector) and so, when scanning in Contact Mode, it is expected that the deflection of all 3 cases to be equal (to the setpoint). In order to keep this deflection constant, the microscope lowers or raises the cantilever, thus diminishing or increasing the normal force. As a consequence, for case Fig 9b to have the same deflection as in Fig 9a, the cantilever will need to be raised, lowering the normal force. While in Fig 9c, the cantilever will need to be lowered, to increase the normal force and achieve the expected cantilever bending (setpoint).

Although there is no height difference on the surface, in Fig 9b the surface will appear to be higher, and in Fig 9c it will appear to be lower than it really is. As a consequence, in a sample surface with two regions with different frictional coefficients: one very high, while the other very low, in the low friction coefficient region, the cantilever will behave as image Fig 9a, while in the high friction coefficient region, it will behave as Fig 9b or Fig 9c, depending on the scanning direction (backward or forward). In such a case, a completely flat region, but

with different frictional coefficients may appear as a hole or as a hill in the topography image depending on scanning direction used.

## 2.2 – Experimental Results

An experiment was carried out in order to verify this artifact using the setup of Fig 10: a graphene monolayer ($\sim 1nm$) is on top of a wafer of silicon with a layer ($\sim 300nm$ thick) of silicon oxide. Graphene has a very low frictional coefficient [57–61] (as does graphite [62–64]), while silicon oxide has a larger friction coefficient with the AFM tip ($\mu_s = 0.48$) [65]. A cantilever was used to scan in the parallel scan direction and both channels of topography (backward and forward) are acquired. The experiment was done with increasing setpoints ("forces") and the graphene height is measured in each step[4]. Subsequently, the same experiment is repeated, with the same forces, but in the perpendicular scanning direction and the results are summarized in Fig 11.

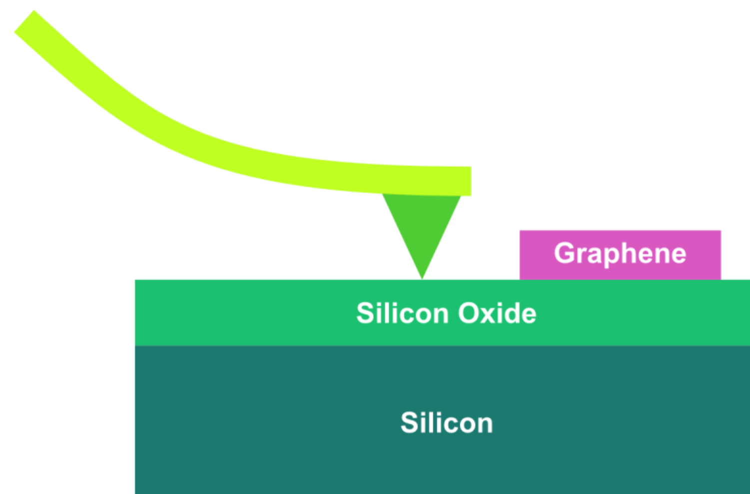


***Fig 10***. *Side view of the experimental setup. A monolayer graphene is on top of a thick layer of silicon oxide in a silicon substrate.*

[4] The graphene height is measured as the difference of topography signal of the graphene to the silicon oxide (i.e. the height measurement is relative to the silicon oxide). The height is measured as the mean height of an certain area on top of the graphene and silicon oxide.

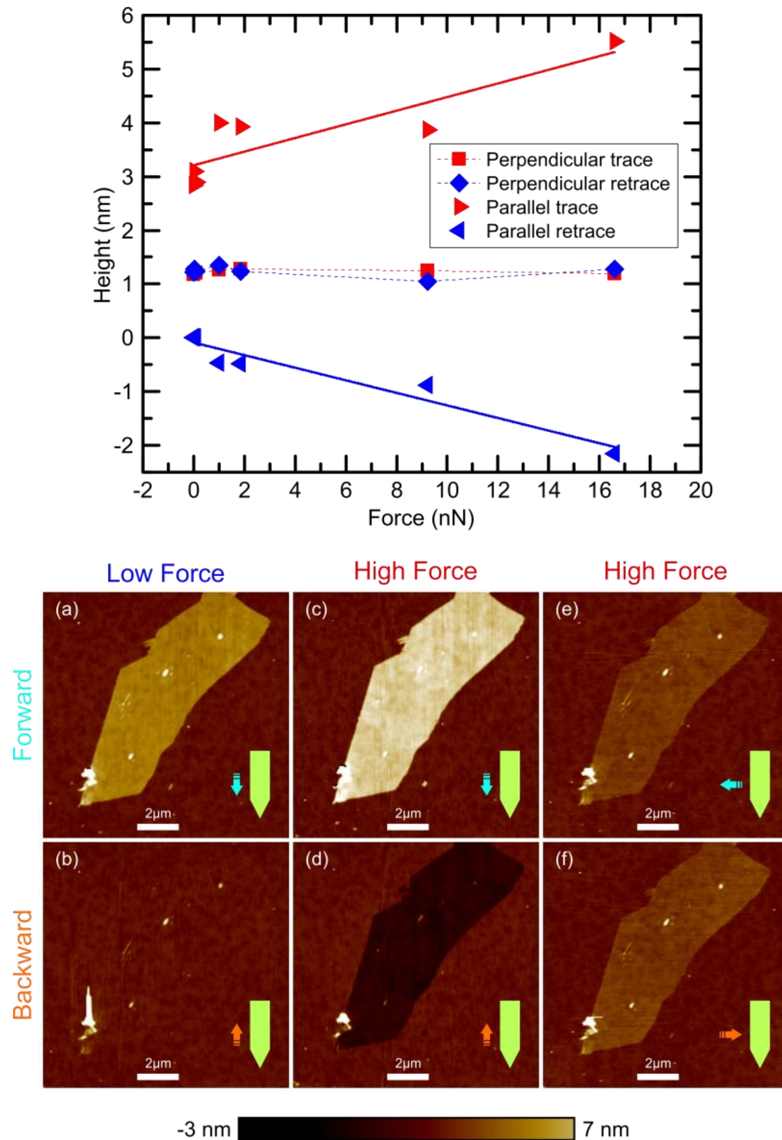


***Fig 11****. Top Panel: Experimental data of the height of the graphene in function of the setpoint (force) for 4 different scans. Both forward (trace) and backward (retrace) scanning directions for the perpendicular and parallel directions. The thick red and blue line consists of a liner fit of the data. Bottom Panel: Topographic image of the graphene used in the experiment. (****a****,****b****) constitute a low force regime for the parallel geometry, (****c****,****d****) constitute a high force regime for the parallel geometry, (****e****,****f****) constitute a high force regime for the perpendicular geometry.*

As shown in Fig 11, the graphene layer appears either as higher or lower in the parallel scan direction, and its height increases/decreases with the applied force. But, in the perpendicular scan direction, the graphene height is constant, regardless the force or scan direction used. In section 2.1 – Qualitative Understanding, it is explained that regions with high friction appear higher in the backward direction (the scanner need to be raised) while regions with high friction in the forward direction appear as lower (the scanner need to be lowered). But in Fig 11 the graphene height in the backward direction is being decreased,

while the height in the forward direction is being increased: apparently, the opposite of what is explained in 2.1 – Qualitative Understanding. The reason for this is very simple: graphene has almost no frictional coefficient, so its height will be practically equal in both forward and backward directions. What is really happening is as follows: the silicon oxide substrate is appearing as higher in the backward direction, but the graphene stays the same height, so as a net result, the height of the graphene minus the height of the silicon is decreased. For the forward direction, it is the opposite: the silicon is appearing lower, but the graphene is at the same height, so the height difference between the two appears greater. So it is not actually the graphene that is changing (or appearing to change) its height, but the silicon oxide substrate itself. The artifact occurs when there are regions with different frictional coefficients, affecting more regions with higher friction.

In the parallel scan of Fig 11, no artifact is expected at zero force, since zero force means no friction (assuming a standard model of friction $F_{fric} = \mu N$, where $N$ is the normal force). But, as shown, the graphene height is changed even with low (zero) force. But even in low forces, there still exists a force of adhesion (capillary forces) caused by the water meniscus (Fig 8). This force is caused by a thin water meniscus formed due to impurities, air humidity, etc [2,3,5,7]. When moving the cantilever, the tip is dragging this meniscus, thus exerting a force (a frictional force) and this is why there is an artifact even with low forces. Since the artifact occurs even with low forces, this additional force is enough to yield significant contributions.

This is a remarkable result due to the cantilever used, with a very large length (374 μm). And, as will be seen later (section 2.3.3 – Topography Artifact), the greater the length of the cantilever, the more pronounced will be the artifact.

Fig 11 shows that these additional frictional forces caused by adhesion do not affect the height of the graphene in perpendicular scanning, and that its height is constant. And this height is the true height of the graphene.

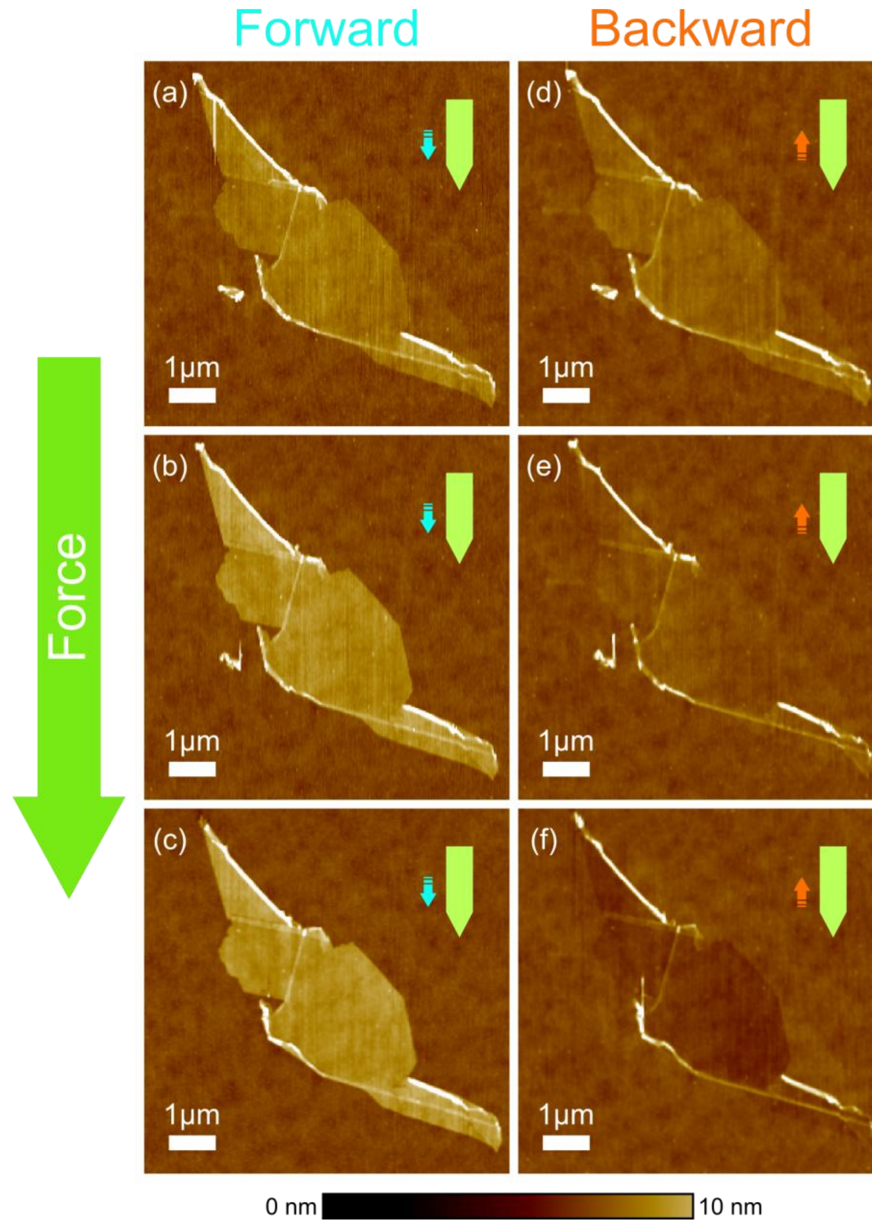


***Fig 12***. *Topographic image a graphene flake under different scanning forces in a parallel scanning. (**a-c**) constitute a topographic image of the forward direction while (**d-f**) the backward direction for a parallel scan direction. In (**a**) and (**b**) have normal force of 2 nN; in (**c**) and (**d**) of 59 nN; in (**e**) and (**f**) of 157 nN. As can be seen from (**a-f**) the graphene appears as a hole in the backward direction (**d-f**) and gets higher in the forward direction (**a-c**).*

Fig 12 shows the graphene (topography) under different scanning forces in a parallel scanning configuration. Figures **a-c** constitute topographic images of the forward direction, while **d-f,** the backward direction. Images **a** and **b** have a normal force of 2 nN; **c** and **d** of 59 nN; **e** and **f** of 157 nN. As can be seen from images **a-f**, the graphene appears as a hole in the backward direction **d-f** and gets higher in the forward directions **a-c**. These images were acquired with a short cantilever and with a high spring constant, so there would be (almost) no

artifact in low forces, but there would still be an artifact with higher forces. Here, the frictional forces caused by the adhesion forces are not enough to cause substantial artifacts in low force, but are still present and change the topography slightly.

The experimental difficulties in dealing with high forces are that the graphene may break or curl on itself, as shown in the lower right of Fig 12.

This artifact is a serious issue, principally in recent years, with the advances in two dimensional materials [25]. Although the Contact Mode is being used less often than in the early days of AFM, as it is preferable to use less intrusive techniques as the Non-Contact Mode, or the Tapping Mode [4,5], it is still a useful tool for nanomanipulations [2,3,5]. As the tip is in hard contact with the surface, it is possible to modify it by applying different forces on certain regions, therefore modifying it locally. If any artifact is produced during these nanomanipulations, the results become non reproducible, or biased to a particular direction used. Since not only the topography is affected, the normal force also changes from scanning angle, the forces being reported on a nanomanipulation experiment may underestimate or overestimate the real applied force.

## 2.3 – Analytical Theory

The study of the deformation of a cantilever can be found in any book about Structural Mechanics, Mechanics of Materials or Structural Engineering [26–30,50–56,66–83]. Here, it will be derived the cantilever deformation when there is a load applied to its tip. It will only be considered a deformation by a force along the axis of the cantilever (a parallel geometry), since, in this case, there is no torsion and the model simplifies drastically (and the artifact can still be accounted for).

### 2.3.1 – Euler-Bernoulli Beam Theory

The Euler-Bernoulli Beam Theory [50,51,53–56,66] will be used for the bending deformation. The geometry of the cantilever is shown in Fig 13: notice the tip of the cantilever is a square pyramid. This model is used since it is the simplest to implement and the geometric factors of the tip are absent: it is only specified by the tip height $h_{tip}$. The shape of the tip can slightly change the results, but, here, its effect will be considered irrelevant and

the only important geometric factor of the tip is its height. The cantilever material (usually silicon or silicon nitride) can be a monocrystal or policrystal, it can also be coated with a film (usually gold, for better reflexivity) and the tip can also be coated with a film (magnetic coating, electric coating, etc) and be made of a different material than the cantilever. Thus the cantilever elastic properties will be anisotropic (directional dependent) and will also change from position, since each part of the cantilever has a different material. For simplicity these variations will not be considered, instead the cantilever elastic properties will depended upon only one factor, the Young modulus $E$, or in others words, the cantilever is isotropic and made of the same (mean) material.

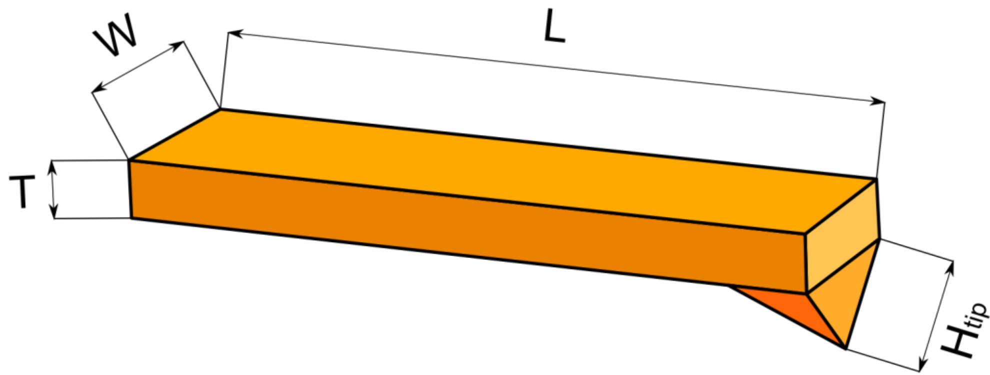


***Fig 13***. *Geometric parameters of the cantilever. $T$ is the cantilever thickness, $L$ is the cantilever length, $W$ is the cantilever width, and $h_{tip}$ is the tip height.*

The principal aspect of the Euler-Bernoulli Beam Theory is that plane sections remain plane and normal to the neutral axis (the neutral axis is an imaginary axis where the stresses are zero).

A deformation of the cantilever results in a strain that can be calculated from this displacement as follows[5]:

$$\varepsilon_{ij} = \frac{1}{2}\left(\frac{\partial u_i}{\partial x_j} + \frac{\partial u_j}{\partial x_i}\right) \tag{1}$$

Where $u_i$ is the displacement of the cantilever in the $i$ direction, $\varepsilon_{ij}$ is the strain tensor and $i, j = x, y, z$ the axis.

---

[5] See Appendix A.

The displacements $u_i$ can be calculated from Fig 14 and Fig 15, where only loads in the $zx$ plane are considered and there is no displacement in the $y$ direction (parallel scan).

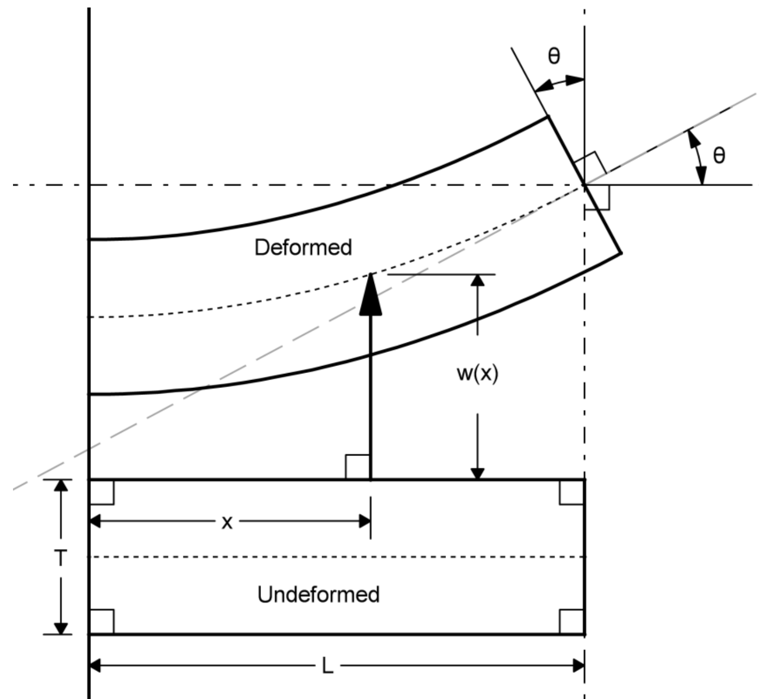


***Fig 14**. Bending deformation of the cantilever. As it can be seen, plane sections remain plane and perpendicular to the neutral axis.*

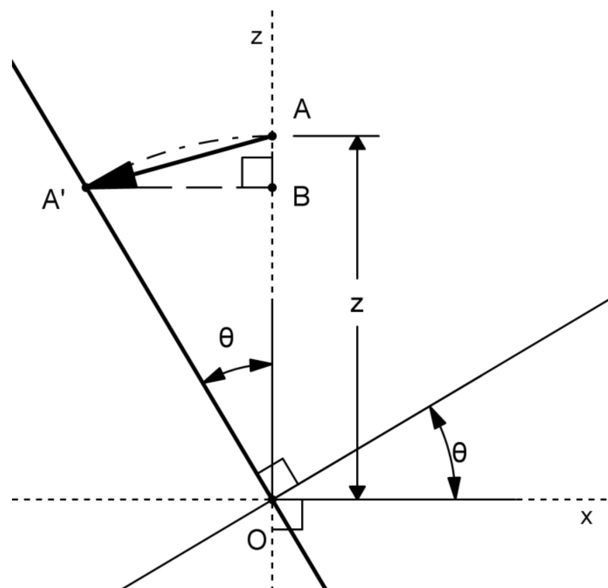


***Fig 15**. Zoom of Fig 14. It shows the displacement vectors from the non-deformed to the deformed geometry.*

In Fig 14, w(x) is the deformation of the neutral axis (dotted line) and $\theta = \arctan w'(x) \cong w'(x)$ is the angle that this curve makes with the horizontal axis.

From Fig 15, the point $A$ is displaced to the point $A'$ and follows that $|OA| = |OA'| = z$, since plane sections remain plane (also for simplicity the Poisson ratio is considered zero). It follows then that $u_x = \overrightarrow{BA'}$ where the $u_x(x, y, z)$ is the $x$ displacement of the element in the position $(x, y, z)$. If bending occurs upward, there is a negative (positive) displacement above (below) the neutral axis. For a downward bending, the opposite behavior is observed.

Since $|BA'| = z \sin\theta$, it follows that $u_x = -z \sin\theta \cong -z\,\theta \cong -z\,w'(x)$. The displacement in the $z$ direction is equal to the displacement of the neutral axis plus the length of the segment $|BA| = z(1 - \cos\theta)$:

$$u_z = w(x) + z(1 - \cos\theta) \cong w(x) \tag{2}$$

Expressing the displacement as a vector (using $\cos\theta \cong 1$ for small angles):

$$\mathbf{u}(x, y, z) = -z\,w'(x)\hat{\mathbf{x}} + w(x)\hat{\mathbf{z}} \tag{3}$$

Using the formula for the strain (1), the only non-null component is $\varepsilon_{xx}$ that is equal to:

$$\varepsilon_{xx} = -z\,w''(x) \tag{4}$$

The cantilever is made of a linear isotropic material and its elastic properties are specified by its Young Modulus $E$. By Hooke's Law, it follows that:

$$\sigma_{xx} = E\varepsilon_{xx} = -E\,z\,w''(x) \tag{5}$$

For concave bending regions above the neutral axis ($z > 0$), the cantilever will be compressed, while regions below it will be expanded, hence the minus sign in $\sigma_{xx}$.

This stress (5) will cause an internal moment $\mathbf{M}$ (torque) calculated with help from Fig 16 to be:

$$\begin{gathered} d\mathbf{M} = \mathbf{r} \times d\mathbf{F} = (x \quad y \quad z) \times (\sigma_{xx} \quad 0 \quad 0)\,dA \\ d\mathbf{M} = (0 \quad z\sigma_{xx} \quad -y\sigma_{xx})\,dA \end{gathered} \tag{6}$$

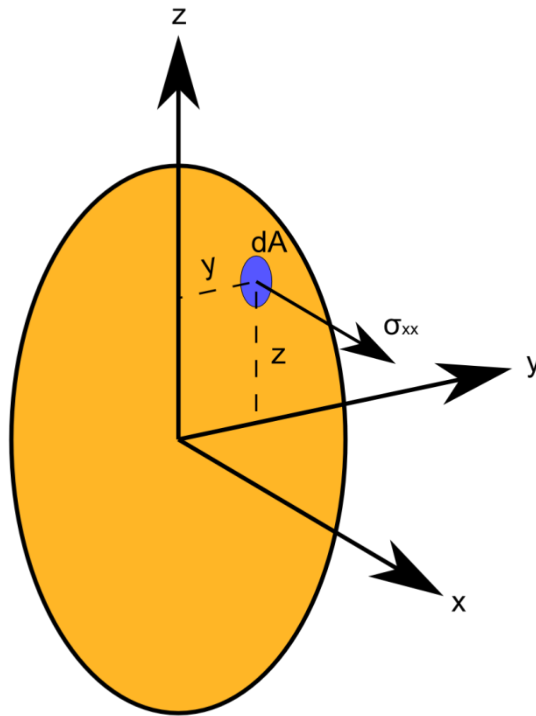


***Fig 16**. Moment created by the stress* $\boldsymbol{\sigma_{xx}}$.

From (6), the $z$ component of this vector may cause a bending in the $y$ direction. However, the only way to create such bending is if there was a force perpendicular to the cantilever ($y$ axis) and such force is absent. Therefore, it will only be considered the moment in the $y$ axis, which causes the bending in the $z$ direction.

Integrating the $y$ component (6), it follows that:

$$M_y = -E\, w''(x) \iint\limits_S z^2\, dA = -EI\, w''(x) \tag{7}$$

Where $I = \iint_S z^2\, dA$ is the moment of area. With the calculations of the internal moment, now the torque caused by the external forces (the forces on the tip) can be calculated for a torque balance equation. The position of the tip in relation of the neutral axis is

$(L \quad 0 \quad -h_{tip}^*)$[6], so the displacement vector of a point on the neutral axis at a distance $x$ from the fixed end is given by $(L-x \quad 0 \quad -h_{tip}^*)$. So the external moment is:

$$\begin{gathered}\mathbf{M} = \mathbf{r} \times \mathbf{F} = (L-x \quad 0 \quad -h_{tip}^*) \times (F_x \quad 0 \quad F_z) \\ \mathbf{M} = -\left(F_x\, h_{tip}^* + F_z\,(L-x)\right)\hat{\mathbf{y}}\end{gathered} \tag{8}$$

Equating the internal (7) to the external moments (8), it follows this differential equation:

$$w''(x) = \frac{F_x h_{tip}^*}{EI} + \frac{F_z}{EI}(L-x) \tag{9}$$

Solving equation with the boundary condition of the cantilever being pinned (i.e. $w(0) = w'(0) = 0$):

$$w(x) = \frac{F_x h_{tip}^*}{2EI} x^2 + \frac{F_z}{6EI}(3L-x)x^2 \tag{10}$$

The difference in the equation (10) and the usual displacement $w$ found in the literature [4,8,84] is the additional term dependent on $F_x$, which is the frictional force.

### 2.3.2 – Constant Deflection

As stated multiple times previously, CM-AFM is a technique of constant deflection, and in AFM, the term deflection is used to mean angle. Since the photodetector measures angle and the setpoint determines a deflection (a signal in the photodetector), a deflection is the same as an angle. As said previously, this angle of deflection $\theta$ is just the derivative of $w$ (i.e. $w'(x)$). This angle changes with the distance, for a setpoint it will be used the angle at the end of the cantilever ($x = L$), since the further away from the cantilever base, the greater the angle is, and since the laser is reflected the cantilever, the greater the angle, the greater the sensibility will be. Equating this deflection $\theta$ with a deflection setpoint $\varphi_s$:

---

[6] $h_{tip}$ is the tip height, while $h_{tip}^*$ is the corrected tip height, the height of the tip from the apex to the neutral axis and is equivalent to $h_{tip}^* = h_{tip} + T/2$, where $T$ is the thickness of the cantilever.

$$\varphi_s = w'(L)$$
$$\varphi_s = \frac{F_x L h_{tip}^*}{EI} + \frac{F_z L^2}{2EI} \tag{11}$$

It will be assumed that the frictional force $F_x$ is proportional to the normal force (Amonton's Law), $F_x = \mu F_z$ [85]. Where $\mu$ is the frictional coefficient and here it will be considered that $\mu > 0$ means a cantilever moving from right to left (backward direction) and $\mu < 0$ indicates a cantilever moving from left to right (forward direction).

The deflection setpoint $\varphi_s$ is defined like it is usually done in AFM, by means of a force curve. In a Force Curve (section 1.5 – Force Curve), the surface is approached on the same point, so the tip does not move quite as much (in the surface plane), so this problem can be regarded as a static one with no friction. In this way, the deflection setpoint can be defined by means of a force setpoint $F_s$, and this force means a normal force that would be done if there were no friction ($F_x = 0$). It then follows from (11):

$$\varphi_s = \frac{F_s L^2}{2EI} \tag{12}$$

The normal force done while scanning at constant deflection can be found by combining (11) and (12) with the friction formula ($F_x = \mu F_z$):

$$F_z = F_s \frac{L}{L + 2\mu h_{tip}^*} \tag{13}$$

The normal force that is expected to be done, $F_s$, is not really the force that is actually being applied, $F_z$. Since the scan direction (the signal of $\mu$) changes this force, the normal force will differ from the backward direction to the forward direction, and none of those will be equal to the setpoint. Moreover, regions with different friction coefficients (modulus of $\mu$) will have different normal forces, even in the same scan direction. Nevertheless, despite the normal force changing from region to region and in each scan direction, the deflection will always stay constant.

The ratio of the normal forces in the backward and forward directions is:

$$\frac{F_{backward}}{F_{forward}} = \frac{F_z|_{\mu>0}}{F_z|_{\mu<0}} = \frac{2L}{2|\mu|h_{tip}^* + L} - 1 \tag{14}$$

This ratio is always less than 1, so in the backward direction the normal force is always smaller than the forward normal force. In the backward direction, the frictional forces will bend the cantilever more, so the normal force will be smaller, while in the forward direction, the frictional forces will unbend the cantilever, so the normal forces will be greater.

### 2.3.3 – Topography Artifact

The formula for the cantilever (3) is:

$$\mathbf{u}(x, y, z) = -z\, w'(x)\hat{\mathbf{x}} + w(x)\hat{\mathbf{z}} \tag{3}$$

Since the tip is in contact with the surface, it is important to know how it moves. Substituting $w, F_x, F_z$, (equations (10) and (13) and evaluating it on the tip $\left(x = L, y = 0, z = -h_{tip}^*\right)$.

$$\mathbf{P}_{\text{tip}} = \mathbf{u}\left(L, 0, -h_{tip}^*\right) = F_s \frac{L^2 h_{tip}^*}{2EI}\hat{\mathbf{x}} + F_s \frac{L^3\left(2L + 3\mu h_{tip}^*\right)}{6EI\left(L + 2\mu h_{tip}^*\right)}\hat{\mathbf{z}} \tag{15}$$

Comparing the $z$ displacement of the tip, $\mathbf{P}_{\text{tip}}$, from a region with friction to a region without friction, as this matches the experimental setup shown in section 2.2 – Experimental Results, where the tip moves from silicon oxide to graphene:

$$\Delta h = \left(\mathbf{P}_{\text{tip}}\big|_{\mu} - \mathbf{P}_{\text{tip}}\big|_{\mu=0}\right) \cdot \hat{\mathbf{z}} = -F_s \frac{L^3 \mu h_{tip}^*}{6EI\left(L + 2\mu h_{tip}^*\right)} \tag{16}$$

It should be noted that there is no loss of generality when assuming one region is frictionless. In order to get the height difference between two regions of non-null friction coefficients, $\Delta h|_{\mu_1} - \Delta h|_{\mu_2}$ can be used instead of (16).

The experimental result Fig 11 (showed again in Fig 17 the top panel for the parallel direction) shows that the artifact becomes more positive with the force in the forward (trace) direction ($\mu < 0$) and more negative in the backward (retrace) direction ($\mu < 0$). From the formula of $\Delta h$ (16), if follows that $\Delta h > 0$ for $\mu < 0$ and $\Delta h < 0$ for $\mu > 0$, as expected from the experiment.

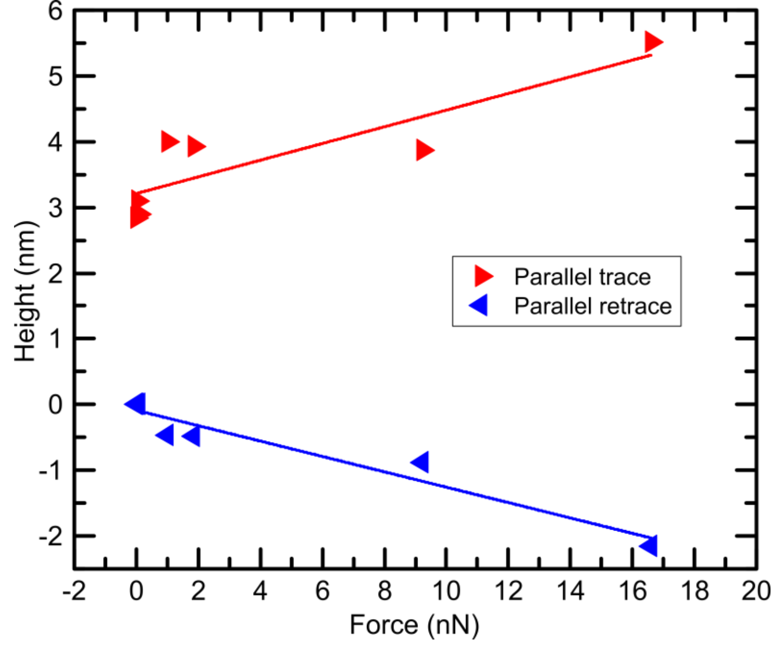


***Fig 17***. *Experimental data of the height of the graphene in function of the setpoint (force) for 2 different scans. Both forward (trace) and backward (retrace) scanning directions for the parallel directions. The liner fit for the red curve (trace) is* $h = 3.21 + 0.13F$ *and for the blue curve (retrace)* $h = -0.088 - 0.12F$*, where h is the graphene height (in nanometers) and F is the force (in nanonewtons).*

It is more usual to use the spring constant $k$ instead of the Young modulus $E$ when dealing with AFM, also it is preferable to use the geometric parameters of the cantilever instead of the moment of area $I$. The moment of area is $I = \iint z^2 dA = (T^3 W)/12$. By means of Hooke's Law in absence of friction, the spring constant can be calculated; $F_s = kw(L)$ which can be solved for $k = 3EI/L^3$. Making these substitutions on $\Delta h$ (16) and using the fact that $h_{tip}^*$ is small compared to $L$ it follows that:

$$\Delta h = -F_s \frac{\mu h_{tip}^*}{2kL} \tag{17}$$

Using the experimental cantilever parameters (length: 374 µm, width: 26 µm, spring constant: $0.075\ \mathrm{nN/nm}$), if follows that:

$$\Delta h = -0.3 \mu F_s \tag{18}$$

Which, in comparison to the experimental data, gives a frictional coefficient of 0.4 to the silicon oxide. The value $\mu$ found using this equation is not actually the friction coefficient of the silicon oxide, but rather the difference of friction coefficients of both materials. A formula that better express the artifact for regions with non-zero friction coefficient is:

$$\Delta h = -F_s \frac{h_{tip}^{*}}{2kL} \Delta \mu \quad (19)$$

## 2.4 – Numerical Results

In this section is shown the simulation results of the cantilever deflection, where the simulation is done with Comsol Multiphysics 4.4, a finite element package for numerical simulation of differential equations.

### 2.4.1 – Finite element method

The finite element method is a numerical technique to solve differential equations using variational methods (minimizing an error function). It works by dividing the geometry of the problem being studded in small elements (subdomains) consisted of polygons (Fig 19), and the vibrational integrals are solved for each element.

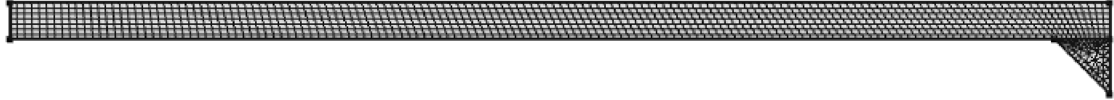

***Fig 18**. Geometry meshed with quadrilaterals (beam's body) and triangles (cantilever tip).*

For the sake of demonstration here will be shown briefly how this is done for the Poisson equation $\nabla^2 \emptyset = -f$ (it can be done for any differential equation, but the Poisson equation is one of the simplest examples). To make a variational formulation of the problem this equation need to be cast in the weak form, where the differential equation is not required to hold absolutely; for it we multiply it by a test function, $\delta u$, which is an arbitrary function that is zero on the boundaries, and integrate on the domain.

$$\int_{\Omega} \nabla^2 \emptyset \delta u dV = -\int_{\Omega} f \delta u dV \quad (20)$$

Using integral by parts (green first identity) on the first integral and using the fact that $\delta u$ is zero at the boundary:

$$\int_{\Omega} \nabla \emptyset \cdot \nabla \delta u dV = \int_{\Omega} f \delta u dV \quad (21)$$

The test function $\delta u$ is chosen in such a way to be non-zero only at an element (polygon), when the test function has this property it is called the basis. In this way the integral (21) is calculated for each element. Choosing a set of basis functions (test functions) for all elements, we have a set of equations, these equations can be put into a matrix form and solved using any method to solve matrix equations. In Comsol there are two branches of solvers to solvers for problems like this, they are the direct method and the interactive method. The major differences between them are that direct methods usually uses more memory, but they solve the problem in a single step (basically calculating the inverse of matrix equation) and the interactive method, that uses less memory but requires the interaction of the solution until convergence. In this dissertation all simulations are run using the direct method using the solver MUMPS (MUltifrontal Massively Parallel sparse direct Solver).

### 2.4.2 – Cantilever Model

A series of simulations were done using Comsol Multiphysics 4.4 using the module of Structural Mechanics in both 2D and in 3D. The Beam Module[7] was also used to better compare the results of the Euler-Bernoulli model (a more in depth description of these models are done in the Theory chapter).

A typical contact cantilever is simulated (length of $300\mu m$, width of $30\mu m$, thickness of $4\mu m$, tip height of $12\mu m$) with a maximum force applied of $100nN$. The Young modulus of the cantilever is adjusted to give a spring constant of $1\,nN/nm$ for simplicity (since the model is linear in the loads, these conversion constants are unimportant for the result and only useful for a better view of the simulation). The cantilever is considered isotropic, for a comparison between an isotropic and anisotropic model see Appendix B.

Three forces are acting on the tip of the cantilever along the 3 axis (Fig 19a). Since these forces cause a moment (torque) on the cantilever that further causes it to bend and be

[7] The beam modulus uses the Euler-Bernoulli beam equations and gives the same results as the Structural Mechanics module. Its great advantage is its computational speed, since there are far less degrees of freedom. Specific data from the beam modulus are not shown, but give the same behavior with the same precision as the Structural Mechanics modulus.

torsioned, they are subdivided in further cases. The force perpendicular to the axis ($F_y$) along the surface can cause a torsion of the cantilever and can also bend it, so this force is divided in 2 cases: a torsion one (where there is no bending, Fig 19d) and a bending (where there is no torsion, Fig 19e). The force along the axis of the cantilever ($F_x$) can compress[8] the cantilever and also bend it (Fig 19b). The compression will be orders of magnitude smaller than any other displacement, and the effect will be dominated by the bending of the cantilever. The normal force ($F_z$) can cause only bending (Fig 19c), so there are 4 cases to simulate: 3 bending and 1 torsion.

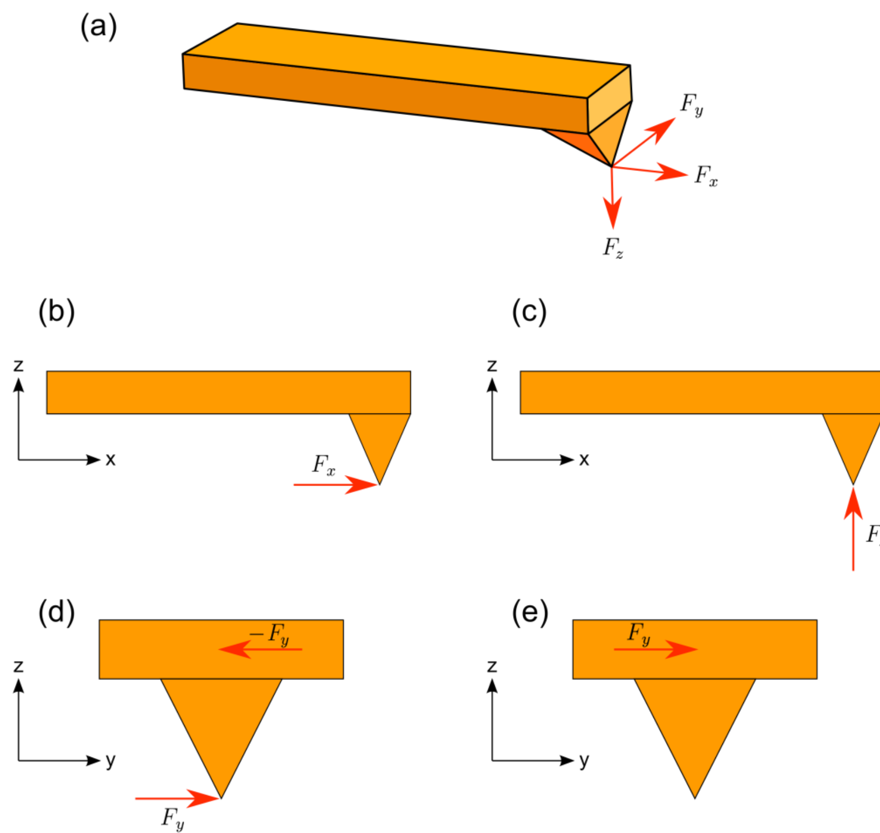


***Fig 19***. *Scheme of the 4 cases to simulate. (**a**) consists of three forces acting on the tip, (**b**) consists of the force $F_x$, (**c**) consists of the force $F_z$, (**d**) consists of the force $F_y$ in the torsion case, (**e**) consists of the force $F_y$ in the bending case.*

[8] A force along the axis of the cantilever can also cause a compression of the cantilever along its axis. This compression will not deform the cantilever along directions perpendicular to its axis, unless the force is excessive, then it will also cause buckling and possible failure of the cantilever. This deformation at the end of the cantilever be proportional to $T^2/3kL^2$ times the force, which is a very small quantity ($\sim 4 \times 10^{-4}\, nm/nN$). For its derivation see Appendix C

Since the model is linear, the principle of the superposition can be used to simulate each case separately and their net effects combine. In this way, the general case of an arbitrary load on the tip in an arbitrary direction (this is done also in the theory) can be considered. Also, it is only necessary to simulate positive or negative forces, since the model is linear and the displacements are zero at zero force, so the displacements need to be asymmetric at zero (odd function), as indeed they are.

### 2.4.3 – 3D Simulation

Fig 20 shows the results of the simulation. The color map of the cantilever indicates the von Mises stress [67–70] on in, which gives information of an equivalent stress acting at that point by all forces (normal and shear stresses) in all directions; since the von Mises stress is not an absolute measure, it was normalized for each simulation (a-b). The von Mises stress can be only compared within each case (simulation). Fig 20a show the deformation with a force $F_x$ applied on the tip (Fig 19b scheme), it will causes a bending on the bean, displacing it upwards ($z$ direction). In Fig 20b there is a force $F_z$ on the tip (Fig 19c scheme), that will also causes an upward bending. In Fig 20c there is a force $F_y$ on the tip and a force $-F_y$ on the neutral axis (Fig 19d scheme), that rotates the cantilever along its axis. In In Fig 20d there is a force $F_y$ on the neutral axis (Fig 19e scheme), that causes a bending in the $y$ direction. It can be seen from these pictures that deflection on the $z$ axis will be maing dominated by the forces $F_x$ and $F_z$ (Fig 19b,c scheme), as will be seen shortly later.

In Fig 20 it can also be seen that the point where the load (the tip or the neutral axis) is applied has higher stress. This is expected, since the simulation was done with a point load. However, according to Saint-Venant's Principle [31,32,86], the difference of a point load (idealized) and a distributed load (reality) becomes small the further away from the load, so the displacements along the beam are more accurate, while the displacements near the tip are less accurate because of the point load. The simulation could have been done using a distributed load on the area of the tip head, but since this area is very small (typical radius of the tip is $\sim 10nm$) in comparison with the whole model, the distributed load will be approximately an idealized point load (the ratio between volume of the tip head to the whole tip is a very small), therefore a point load where chosen.

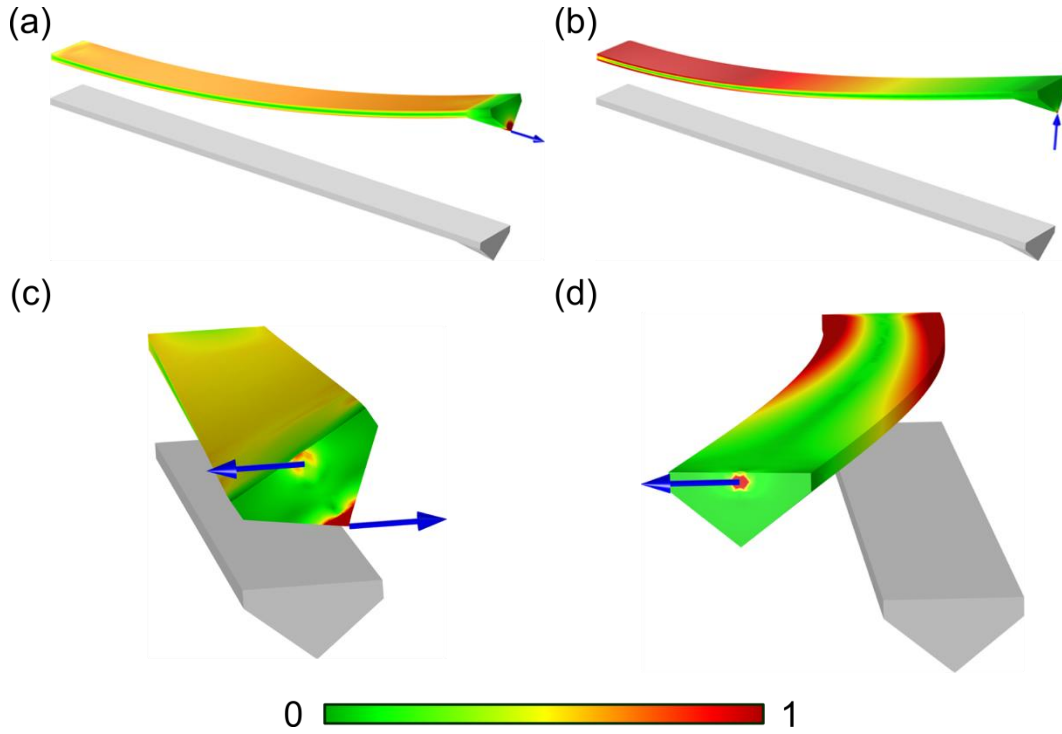


***Fig 20***. *Von Mises stress on the cantilever for the 4 cases shown in Fig 19. (**a**) force $F_x$ on the tip in bending case (Fig 19b), deformation factor* $7000$*; (**b**) force $F_z$ on the tip in bending case (Fig 19c), deformation factor* $600$*; (**c**) force $F_y$ on the tip and on the neutral axis in the torsion case (Fig 19d), deformation factor* $20000$*; (**d**) force $F_y$ on the neutral axis in the bending case (Fig 19e), deformation factor* $25000$*. The scale of the von Mises stress distribution is normalized from* $0$ *to* $1$.

The main difference between the bending of the forces $F_x$ and $F_z$ (Fig 20a,b) is the scale of the deformation (deformation factor), which are $7000$ and $600$ respectively. This deformation factor is how much the displacements are exaggerated in the figure, since these displacements are in the nanometer range and the geometry is in the hundreds of micrometers range, for visualization purposes, the displacements need to be exaggerated for better visualization. As can be seen, the force $F_x$ causes displacements one order of magnitude smaller than the force $F_z$. The ratio between the two displacements at the tip (caused by a force $F_z$ over the one caused by the force $F_x$) can be calculated as follows (see section 2.3.1 – Euler-Bernoulli Beam Theory):

$$\frac{u_z|_{F_x=0}}{u_z|_{F_z=0}} = \frac{2L}{3h_{tip}^*} \tag{22}$$

Also we can see the differences between the bending and torsion cases for the force $F_y$. In the general case Fig 19a, this force $F_y$ will case both bending and torsion. By applying a counteracting force on the neutral axis (Fig 20c) it is possible to eliminate the bending (sum

of forces will be zero) and get only the torsion, analogous by applying only one force on the neutral axis (Fig 20d) it is possible to get only the bending case. The combined effect is the sum of both effects.

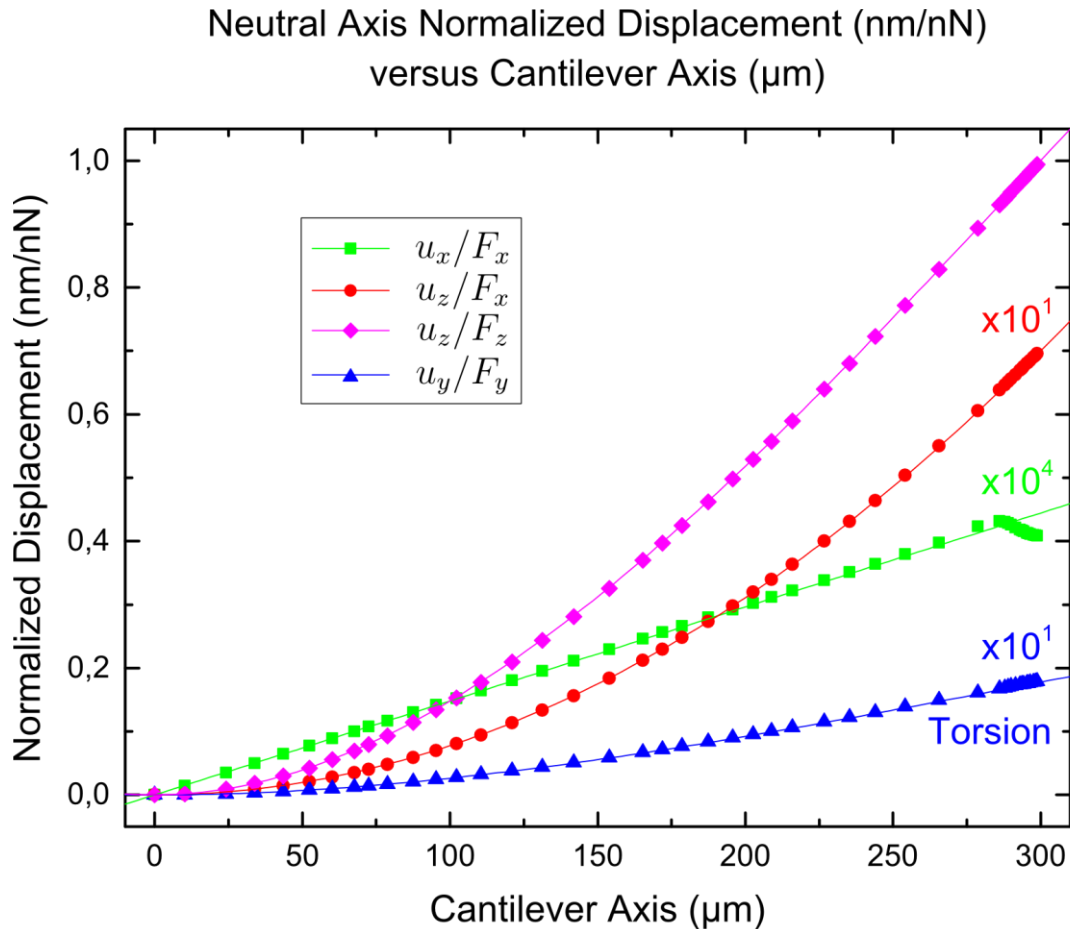


*Fig 21. Neutral axis normalized displacement (displacement divided by force) in function of the length along the cantilever. A dot consists of the numeric data while a solid line is the respective analytical formula plotted. Green curve consists of the normalized displacement $u_x$ for the force $F_x$; blue curve consists of the normalized displacement $u_y$ for the force $F_y$ for the bending case; red curve consist of the normalized displacement $u_z$ for the force $F_x$; magenta curve consists of the normalized displacement $u_z$ for the force $F_z$. Analytical formulas used are given in Table 1.*

In order to better understand the cantilever deformation, the $x, y, z$ deformation of the cantilever with the forces $F_x, F_y, F_z$, will be plotted. Fig 21 show the normalized displacement[9] in function of the length along the cantilever ($x$ axis). The displacements not shown for a given force are small and in the limit of the error of the simulation. The displacement $u_x$ for

[9] Displacement per applied force, since the model is linear for a ramp of forces, they give the same normalized displacement.

the force $F_x$ constitute the case of compression of the beam (Fig 21 green curve), since the bending of the beam will give a $x$ displacement (3) $u_x = -zw'(x)$, and since the graph is evaluate at the neutral axis, $z = 0$, bending will not cause $x$ displacement. As can be seen, this displacement is very small, and compression can be safely disconsidered, as was done in the theory. The $u_z$ displacement for the force $F_x$ (Fig 21 red curve) and for the force $F_z$ (Fig 21 magenta curve) shows how the cantilever is deformed (its profile). The displacement will be dominated by the force $F_z$, as can be seen from (23). The $u_y$ displacement caused by the force $F_y$ in the bending case (Fig 21 blue curve) is also very small. The bending profile is very similar to the profile of the displacement $u_z$ for the force $F_z$, as they follows from the theory by interchanging the thickness with the height of the cantilever (Table 1), the reason being that it gives far less displacement is that the cantilever is far wider than it is thicker. The analytical formulas are shown in Table 1.

| Displacement | Caused by Force | Analytical Formula |
|---|---|---|
| $\boldsymbol{u_x}$ | $F_x$ (compression) | $F_x \frac{T^2}{4kL^3} x$ |
| $\boldsymbol{u_z}$ | $F_x$ (bending) | $F_x \frac{3h^*_{tip}}{2kL^3} x^2$ |
| $\boldsymbol{u_y}$ | $F_y$ (bending) | $F_y \frac{T^2}{2kL^3W^2}(3L - x)x^2$ |
| $\boldsymbol{u_z}$ | $F_z$ (bending) | $F_z \frac{1}{2kL^3}(3L - x)x^2$ |

***Table 1***. *Analytical formulas used in Fig 21 for the neutral axis displacement. Derivation follows directly from section 2.3.1 – Euler-Bernoulli Beam Theory.*

Another piece of information of interest is the position of the tip. Since the tip is in constant contact with the surface, it is important to know how it is displaced. The $z$ position of the tip should be constant along a flat surface (it does not leave the surface), so the amount of the tip displacement in a constant deflection mode shows how much the scanner will compensate so the tip does not move. In practice, the scanner moves the base of the cantilever, but in the theory the base is pinned (it does not move). So, to convert theory to reality, it is necessary to translate the cantilever in such a way for the tip to be constantly in contact with the surface, simulating, therefore, a real scan where the scanner is really moving the cantilever. Fig 22 shows the tip displacement versus force applied, The force $F_y$, either in

bending or torsion cases will only causes a displacement in the $y$ axis (Fig 22 red and magenta curve respectively). The forces $F_x$ and $F_z$ will causes a displacement both will cause a displacement in the $z$ axis (Fig 22 blue and red curve respectively), they will also cause a displacement in the $x$ axis, not shown here (since they follow directly from the relationship (3) $u_x = -zw'(L)$) and are trivially related. All others displacements are zero for all others forces. So as saw earlier from Fig 21, only the forces $F_x$ and $F_z$ will change the $z$ position of the cantilever. And there is a great agreement between analytical formulas and numerical results. Analytical formulas are shown in Table 2, notice that the displacement $x$ caused by the force $F_z$ is the same at the tip as the displacement $z$ caused by the force $F_x$, this by no means denote that the displacements elsewhere are equal, as can be seen from Fig 21. Analytical formulas for $y$ displacement caused by the force $F_y$ in the torsion case is not calculated because it requires sophisticated torsion theory such as St. Venant Torsion Theory [76–79] or Prandtl Torsion Theory [26,80–83], and since we are only interested in $z$ displacements for the artifact, and this torsion does not gives any such displacements, and thus were not considered in the analytical theory in section 2.3 – Analytical Theory.

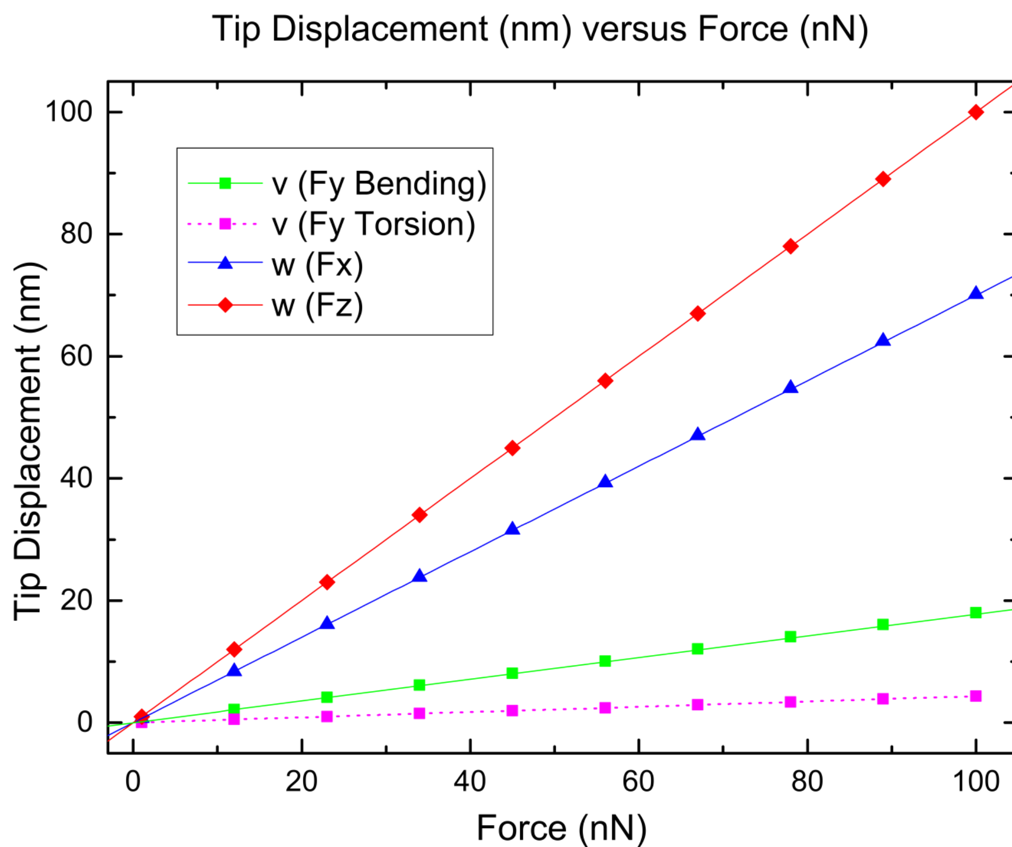


*Fig 22. The displacement at the tip in function of the force applied. A dot consists of the numeric data while a*

*solid line is the respective analytical formula plotted. Red curve consists of the tip displacement $u_z$ for the force $F_z$; blue curve consists of the tip displacement $u_z$ for the force $F_x$; green curve consists of the tip displacement $u_y$ for the force $F_y$ for the bending case; magenta curve consists of the tip displacement $u_y$ for the force $F_y$ for the torsion case. The forces $F_x$ and $F_z$ also causes a displacement $u_x$, but it is now shown. See Table 2.*

| Displacement | Caused by Force | Analytical Formula |
|---|---|---|
| $u_x$ | $F_x$ (bending) | $F_x \frac{3{h^*_{tip}}^2}{kL^2}$ |
| $u_x$ | $F_z$ (bending) | $F_z \frac{3h^*_{tip}}{2kL}$ |
| $u_y$ | $F_y$ (bending) | $F_y \frac{T^2}{kW^2}$ |
| $u_z$ | $F_x$ (bending) | $F_x \frac{3h^*_{tip}}{2kL}$ |
| $u_z$ | $F_z$ (bending) | $\frac{F_z}{k}$ |

***Table 2***. *Analytical formulas used in Fig 22 for the tip displacement. Derivation follows directly from section 2.3.1 – Euler-Bernoulli Beam* Theory.

The results are summarized in the Table 3, which gives the $x, y, z$ displacements for the forces $F_x, F_y, F_z$ applied both on the tip and the neutral axis. As can be seen analytical theory is in very good agreement with the numerical results, the particular case solved in the theory (no force along $y$ considered) by no means restrict the description of the artifact.

| Point Applied | Force | $u_x$ | $u_y$ | $u_z$ |
|---|---|---|---|---|
| Neutral Axis | $F_x$ | Y* | N | Y |
| Neutral Axis | $F_y$ | N | Y | N |
| Neutral Axis | $F_z$ | N | N | Y |
| Tip | $F_x$ | Y | N | Y |
| Tip | $F_y$ | N | Y | N |
| Tip | $F_z$ | Y | N | Y |

***Table 3***. *Displacements along the $x, y, z$ axis for the forces $F_x, F_y, F_z$ for the neutral axis (top) and for the tip (bottom). Case marked * is for the compression of the cantilever, which is very small.*

### 2.4.4 – Constant Deflection (2D)

Since, as shown in previous section (2.4.3 – 3D Simulation), the only important forces in the creation of the topography artifact are the $F_x$ and $F_z$ in the parallel scan direction, then, performing a 2D simulation (a slice of the 3D model) is enough to investigate all the relevant effects. Doing so has great computational advantages, since convergence in a 2D model is considerably faster than a 3D model. The 2D simulations were done based on the 3D simulations with same parameters and the results compared with the theory. The displacements found in the 2D simulation are the same as the 3D simulation (Fig 21 and Fig 22), and hence are not shown.

The AFM operation in contact mode will them be simulated. For this it will be assumed that the frictional force ($F_x$) along the cantilever axis is proportional to the normal force ($F_z$); i.e., the standard formula for friction, $F_x = \mu F_z$ is assumed to hold [85]. Negative values of $\mu$ will be allowed to simulate both scans directions: forward and backward[10]. The simulation is run in such a way that the normal force $F_z$ is modified in order to keep the deflection constant, while the friction coefficient $\mu$ is being ramped up (in Comsol this is done by means of a Global Equation). In this way, a constant deflection can be attained with varying normal and frictional forces. The deflection angle is calculated from the curl of the displacement and the simulation is run in such a way to make this angle equal to 0.01°.

Fig 23 shows how the vertical displacement $u_z$ (red curve) and the normal force $F_z$ (blue curve) in function of the frictional coefficient $\mu$. When the cantilever is moving in the forward direction (negative $\mu$), the normal force is greater; while in the backward direction (positive $\mu$), a smaller normal force is observed. The force at $\mu = 0$ is the setpoint and can be defined using a force curve. As it can be seen, it follows the same qualitative behaviors as explained in section 2.1 – Qualitative Understanding. It is remarkable that the normal force can change up to 10% above or below the setpoint depending on the scan direction and frictional coefficient (for this particular cantilever). If a precise force is needed in an experiment, the normal force is being overestimating in the forward direction and underestimated in the

---

[10] For more details see section 2.3.2 – Constant Deflection.

backward direction. As it can be seen, the theory correlates well with the simulation. The vertical displacement (red curve) is a direct evidence of the topography artifact, since it is a constant deflection simulation, and it shows how much, depending on the friction, the scanner will need to travel for it to keep constant deflection.

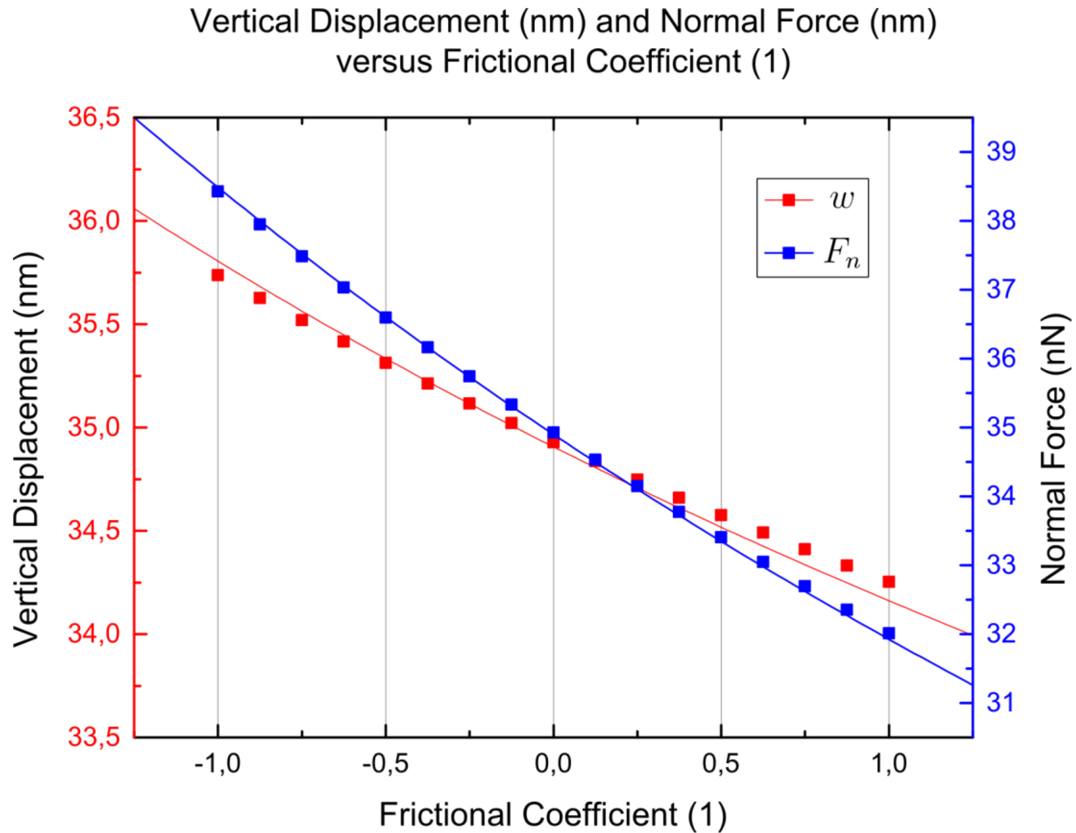


***Fig 23***. *Vertical displacement $u_z$ of the tip (red curve) and normal force $F_z$ (blue curve) in function of the frictional coefficient $\mu$. Positive $\mu$ means backward scan while negative $\mu$ forward scan direction. A dot consists of the numeric data while a solid line is the respective analytical formula plotted.*

The analytical formula for the vertical displacement (Fig 23 red solid line) is (15) and for the one for the normal force (Fig 23 blue solid line) is (13).

Fig 24 shows how the frictional forces can alter the *z* position while maintaining constant deflection and also how the stress changes. In Fig 24a (forward scanning) the cantilever is displaced upwards while in Fig 24c (backward scanning) it is displacement downwards. Fig 24b (no scanning) consists of the setpoint case, where the deflection setpoint is defined in terms of a force (see section 1.5 – Force Curve).

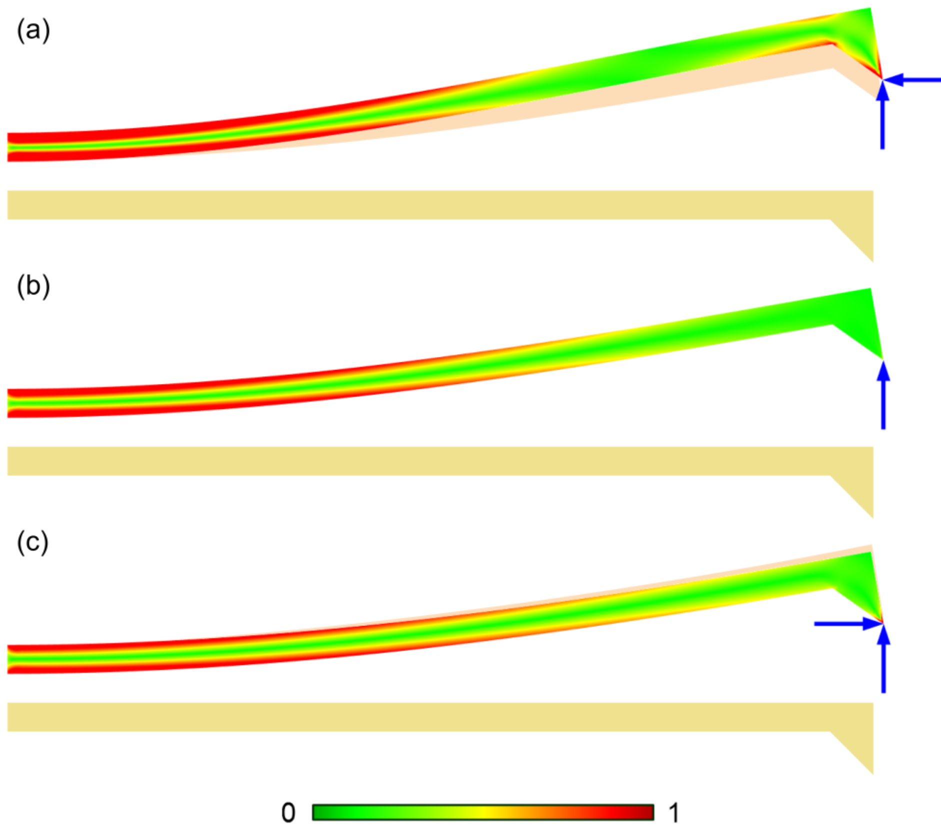


***Fig 24***. *Von Mises stress distribution for different frictional forces applied on the tip while maintaining constant deflection. (**a**) forward scan direction, friction to the left; (**b**) no scanning, no friction; (**c**) backward scan direction, friction to the right. Note: for better visualization the forces on the tip are not to the same scale, they only show direction, not magnitude furthermore, the cantilever thickness is enhanced for better visualization. Also in (**a,c**) a shadow image (**b**) is shown for comparison. The scale of the von Mises stress distribution is normalized from* 0 *to* 1.

## Conclusions

The behavior of an Atomic Force Microscope was investigated, including how the cantilever moves and how this movement is translated into an image. Using the knowledge of the cantilever deformation, it was possible to gain insight on how to properly use the microscope in the Contact Mode, and how this is far from obvious and intuitive in the literature. The lack of understanding of the frictional forces on the parallel scan in the literature was also pointed, as it is usually not mentioned (frictional forces are mainly mentioned only on Lateral Force measurements). Nevertheless, this work shows that the friction plays a major role in image acquisition, giving rise to topographic artifacts when operating in a parallel scan.

Through simulations in Comsol Multiphysics, it was possible to confirm the analytical formulas of the theory. The simulation was of utmost importance for confirming the theoretical prediction of the artifact and to better explain the experimental results, also for highlighting the major factors in the cantilever behavior: the deflection caused by normal forces are about an order of magnitude larger than deflections caused by frictional force. Nevertheless, such frictional forces can still produce height variations in the range of few nanometers depending on the circumstances. Also, the torsion of the cantilever, caused by frictional forces perpendicular to the cantilever, does not produce any additional vertical deflections. Therefore, they create no topographic artifacts and, as a consequence, the perpendicular direction should be the preferred one.

It was also seen that since frictional forces parallel to the cantilever yield additional cantilever deflections and AFM is a technique of constant deflection, these frictional forces act to change the normal force during scan (while maintaining constant deflection). Thus, depending on the scan direction acquired, forward or backward, the topographic image can change substanially. This is a major problem since, in the literature, it is usually not specified which channel was used during image acquisition. Moreover, some microscopes only acquire only a single channel and, since the user has not actually seen the other channel, the artifact my pass unnoticed.

In recent years, Contact Mode has not been used very often, as Non-Contact or Tapping modes [2,4–6,8,9] seem a better choice for topography measurements. Therefore, this artifact

may seem less relevant, but Contact Mode still is a great tool for nanomanipulation and nanomodification. These techniques of modifying matter at the nanoscale require very precise force and positioning controls. If they cannot be controlled precisely, there is little hope of successfully controlling the experiment. Since the major parameter in nanomanipulations is the force being done on the sample surface, if there is no control or methodic way of producing the same force (scan angles may vary during experiments), the results might not be as accurate as expected.

Thus, with the new insight that the preferred way to perform Contact Mode AFM is in the perpendicular direction, where it is possible to avoid any topographic artifacts and, at same time, acquire useful frictional data (using the Lateral Force AFM).

## References


[1] A Practical Guide to SPM (Veeco), (n.d.).

[2] U. Hartmann, An elementary introduction to atomic force microscopy and related methods, 1997.

[3] K.S. Birdi, Scanning Probe Microscopes: Applications in Science and Technology, 2003.

[4] V.L. Mironov, Fundamentals Of Scanning Probe Microscopy, 2004.

[5] B. Bhushan, Nanotribology and Nanomechanics: An Introduction, 2005.

[6] P. Eaton, P. West, Atomic Force Microscopy, Oxford University Press, 2010.

[7] G. Bogdanovic, Surface interactions and adsorbate structures: An atomic force microscopy study, 2002.

[8] D. Sarid, Scanning Force Microscopy: With Applications to Electric, Magnetic, and Atomic Forces, 1991.

[9] R. Howland, L. Benatar, A Practical Guide: To Scanning Probe Microscopy, 1996.

[10] B. Bhushan, Springer Handbook of Nanotechnology, 2004.

[11] a K. Geim, K.S. Novoselov, The rise of graphene., Nat. Mater. 6 (2007) 183–91.

[12] K.S. Novoselov, a K. Geim, S. V Morozov, D. Jiang, Y. Zhang, S. V Dubonos, et al., Electric field effect in atomically thin carbon films., Science. 306 (2004) 666–9.

[13] M. Kawaguchi, S. Kuroda, Y. Muramatsu, Electronic structure and intercalation chemistry of graphite-like layered material with a composition of BC6N, J. Phys. Chem. Solids. 69 (2008) 1171–1178.

[14] M. Engler, B. Ruisinger, Hexagonal Boron Nitride ( hBN ) – Applications from Metallurgy to, (n.d.) 49–53.

[15] Y. Kubota, K. Watanabe, O. Tsuda, T. Taniguchi, Deep ultraviolet light-emitting hexagonal boron nitride synthesized at atmospheric pressure., Science. 317 (2007) 932–4.

[16] J. Lan, J.-S. Wang, C. Gan, S. Chin, Edge effects on quantum thermal transport in graphene nanoribbons: Tight-binding calculations, Phys. Rev. B. 79 (2009) 115401.

[17] J.M. Garcia, U. Wurstbauer, A. Levy, L.N. Pfeiffer, A. Pinczuk, A.S. Plaut, et al., Graphene growth on h-BN by molecular beam epitaxy, Solid State Commun. 152 (2012) 975–978.

[18] A.P.M. Barboza, H. Chacham, C.K. Oliveira, T.F.D. Fernandes, E.H.M. Ferreira, B.S. Archanjo, et al., Dynamic negative compressibility of few-layer graphene, h-BN, and MoS2., Nano Lett. 12 (2012) 2313–7.

[19] S. Koch, M. Langer, S. Kawai, E. Meyer, T. Glatzel, Contrast inversion of the h-BN nanomesh investigated by nc-AFM and Kelvin probe force microscopy., J. Phys. Condens. Matter. 24 (2012) 314212.

[20] L. V. Santos, V.J. Trava-Airoldi, K. Iha, E.J. Corat, M.C. Salvadori, Diamond-like-carbon and molybdenum disulfide nanotribology studies using atomic force measurements, Diam. Relat. Mater. 10 (2001) 1049–1052.

[21] T. Takeno, S. Abe, K. Adachi, H. Miki, T. Takagi, Deposition and structural analyses of molybdenum-disulfide (MoS2)–amorphous hydrogenated carbon (a-C:H) composite coatings, Diam. Relat. Mater. 19 (2010) 548–552.

[22] K. Feng, B. Tang, P. Wu, Selective Growth of MoS2 for Proton Exchange Membranes with Extremely High Selectivity., ACS Appl. Mater. Interfaces. 5 (2013) 13042–9.

[23] J.N. Coleman, M. Lotya, A. O'Neill, S.D. Bergin, P.J. King, U. Khan, et al., Two-dimensional nanosheets produced by liquid exfoliation of layered materials., Science. 331 (2011) 568–71.

[24] S.Z. Butler, S.M. Hollen, L. Cao, Y. Cui, J.A. Gupta, H.R. Gutie, et al., Opportunities in Two-Dimensional Materials Beyond Graphene, (2013) 2898–2926.

[25] X. Song, J. Hu, H. Zeng, Two-dimensional semiconductors: recent progress and future perspectives, J. Mater. Chem. C. 1 (2013) 2952.

[26] P. Kythe, D. Wei, An Introduction to Linear and Nonlinear Finite Element Analysis: A Computational Approach, Springer, 2004.

[27] Y.W. Kwon, H. Bang, The Finite Element Method Using MATLAB, CRC Press, 2000.

[28] T. Chandrupatla, Finite Element Analysis For Engineering & Tech, Universities Press, 2004.

[29] S. Lepi, Practical Guide to Finite Elements: A Solid Mechanics Approach, CRC Press, 1998.

[30] Y.-Q. Long, S. Cen, Z.-F. Long, Advanced Finite Element Method in Structural Engineering, Springer, 2009.

[31] O.A. Bauchau, J.I. Craig, Structural Analysis: With Applications to Aerospace Structures, Springer, 2009.

[32] W.S. Slaughter, The Linearized Theory of Elasticity, Springer, 2002.

[33] U. Hartmann, van der Waals interactions between sharp probes and flat sample surfaces, Phys. Rev. B. 43 (1991) 2404–2407.

[34] U. Hartmann, Manifestation of zero-point quantum fluctuations in atomic force microscopy, Phys. Rev. B. 42 (1990) 1541–1546.

[35] H.-J. Butt, M. Jaschke, Calculation of thermal noise in atomic force microscopy, Nanotechnology. 6 (1995) 1–7.

[36] R. Lévy, M. Maaloum, Measuring the spring constant of atomic force microscope cantilevers: thermal fluctuations and other methods, Nanotechnology. 13 (2002) 33–37.

[37] T. Senden, W. Ducker, Experimental Determination of Spring Constants in Atomic Force Microscopy, Langmuir. 10 (1994) 1003–1004.

[38] J.P. Cleveland, S. Manne, D. Bocek, P.K. Hansma, A nondestructive method for determining the spring constant of cantilevers for scanning force microscopy, Rev. Sci. Instrum. 64 (1993) 403.

[39] J.E. Sader, J.W.M. Chon, P. Mulvaney, Calibration of rectangular atomic force microscope cantilevers, Rev. Sci. Instrum. 70 (1999) 3967.

[40] a. L. Weisenhorn, P.K. Hansma, T.R. Albrecht, C.F. Quate, Forces in atomic force microscopy in air and water, Appl. Phys. Lett. 54 (1989) 2651.

[41] J.L. Hutter, J. Bechhoefer, Calibration of atomic-force microscope tips, Rev. Sci. Instrum. 64 (1993) 1868.

[42] C.P. Green, H. Lioe, J.P. Cleveland, R. Proksch, P. Mulvaney, J.E. Sader, Normal and torsional spring constants of atomic force microscope cantilevers, Rev. Sci. Instrum. 75 (2004) 1988.

[43] S. Jeon, Y. Braiman, T. Thundat, Torsional spring constant obtained for an atomic force microscope cantilever, Appl. Phys. Lett. 84 (2004) 1795.

[44] G. Bogdanovic, A. Meurk, M. Rutland, Tip friction — torsional spring constant determination, Colloids Surfaces B Biointerfaces. 19 (2000) 397–405.

[45] R.S. Gates, J.R. Pratt, Accurate and precise calibration of AFM cantilever spring constants using laser Doppler vibrometry., Nanotechnology. 23 (2012) 375702.

[46] G. Meyer, N.M. Amer, Simultaneous measurement of lateral and normal forces with an optical-beam-deflection atomic force microscope, Appl. Phys. Lett. 57 (1990) 2089.

[47] A. Feiler, P. Attard, I. Larson, Calibration of the torsional spring constant and the lateral photodiode response of frictional force microscopes, Rev. Sci. Instrum. 71 (2000) 2746.

[48] J.M. Neumeister, W. a. Ducker, Lateral, normal, and longitudinal spring constants of atomic force microscopy cantilevers, Rev. Sci. Instrum. 65 (1994) 2527.

[49] R.J. Cannara, M. Eglin, R.W. Carpick, Lateral force calibration in atomic force microscopy: A new lateral force calibration method and general guidelines for optimization, Rev. Sci. Instrum. 77 (2006) 053701.

[50] K.D. Hjelmstad, Fundamentals of structural mechanics, Springer, 2005.

[51] J.J. Connor, S. Faraji, Fundamentals of Structural Engineering, Springer, 2012.

[52] B. Goodwine, Engineering Differential Equations: Theory and Applications, Springer, 2010.

[53] E. Carrera, G. Giunta, M. Petrolo, Beam Structures: Classical and Advanced Theories, John Wiley & Sons, 2011.

[54] N. Jackson, R.K. Dhir, Structural Engineering Materials, CRC Press, 1989.

[55] F. Durka, H. Al Nageim, W. Morgan, D. Williams, Structural Mechanics, Trans-Atlantic Publications, 2010.

[56] W.F. Chen, E.M. Lui, Handbook of Structural Engineering, CRC Press, 2012.

[57] H. Lee, N. Lee, Y. Seo, J. Eom, S. Lee, Comparison of frictional forces on graphene and graphite., Nanotechnology. 20 (2009) 325701.

[58] C. Lee, X. Wei, Q. Li, R.W. Carpick, J.W. Kysar, J. Hone, Elastic and frictional properties of graphene, Phys. Status Solidi. 246 (2009) 2562–2567.

[59] T. Filleter, J. McChesney, a. Bostwick, E. Rotenberg, K. Emtsev, T. Seyller, et al., Friction and Dissipation in Epitaxial Graphene Films, Phys. Rev. Lett. 102 (2009) 086102.

[60] C. Lee, Q. Li, W. Kalb, X.-Z. Liu, H. Berger, R.W. Carpick, et al., Frictional characteristics of atomically thin sheets., Science. 328 (2010) 76–80.

[61] Y. Guo, W. Guo, C. Chen, Modifying atomic-scale friction between two graphene sheets: A molecular-force-field study, Phys. Rev. B. 76 (2007) 155429.

[62] R.H. Savage, Graphite Lubrication, J. Appl. Phys. 19 (1948) 1.

[63] M. Dienwiebel, G. Verhoeven, N. Pradeep, J. Frenken, J. Heimberg, H. Zandbergen, Superlubricity of Graphite, Phys. Rev. Lett. 92 (2004) 126101.

[64] S.W.H. Bragg, An Introduction to Crystal Analysis, 1928.

[65] K. Deng, W.H. Ko, A study of static friction between silicon and silicon compounds, J. Micromechanics Microengineering. 2 (1992) 14–20.

[66] C.M. Wang, J.N. Reddy, K.H. Lee, Shear Deformable Beams and Plates: Relationships with Classical Solutions, Elsevier, 2000.

[67] F.A. Leckie, D.J. Bello, Strength and Stiffness of Engineering Systems, Springer, 2009.

[68] L.M. Surhone, M.T. Timpledon, S.F. Marseken, Von Mises Yield Criterion, VDM Publishing, 2010.

[69] M. Yu, Unified Strength Theory and Its Applications, Springer, 2004.

[70] M.H. Sadd, Elasticity: Theory, Applications, and Numerics, Academic Press, 2009.

[71] Beer, J.& Dewolf, Mechanics Of Materials (In Si Units), Tata McGraw-Hill Education, 2004.

[72] A.K. Singh, Mechanics of Solids, PHI Learning Pvt. Ltd., 2007.

[73] R.K. Bansal, A Textbook of Strength of Materials, Laxmi Publications, 2010.

[74] R.K. Bansal, Engineering Mechanics and Strength of Materials, Laxmi Publications, n.d.

[75] Crandall, Mech Of Solids (Si Units), Tata McGraw-Hill Education, 2008.

[76] W.D. Pilkey, Analysis and Design of Elastic Beams: Computational Methods, John Wiley & Sons, 2002.

[77] K.-E. Kurrer, The History of the Theory of Structures: From Arch Analysis to Computational Mechanics (Google eBook), John Wiley & Sons, 2012.

[78] V. Slivker, Mechanics of Structural Elements: Theory and Applications (Google eBook), Springer, 2006.

[79] A.P.S. Selvadurai, Partial Differential Equations in Mechanics 2: The Biharmonic Equation, Poisson’s Equation, Springer, 2000.

[80] A.P. Boresi, K. Chong, J.D. Lee, Elasticity in Engineering Mechanics, John Wiley & Sons, 2010.

[81] J.R. Barber, Elasticity, Springer, 2009.

[82] R.C. Coates, M.G. Coutie, F.K. Kong, Structural Analysis, CRC Press, 1988.

[83] S.M.A. Kazimi, Solid Mechanics, Tata McGraw-Hill Education, 2001.

[84] D. Sarid, Exploring Scanning Probe Microscopy with MATHEMATICA, 2007.

[85] Y. Mo, K.T. Turner, I. Szlufarska, Friction laws at the nanoscale., Nature. 457 (2009) 1116–9.

[86] M.H. Sadd, Elasticity: Theory, Applications, and Numerics, Academic Press, 2010.

## Appendix A – Infinitesimal strain

Here it will be derived a formula related to the Infinitesimal Strain Theory, available in any good book in Structural Mechanics. A geometric derivation will be given of the relationship between stress and displacement.

In Fig 25 is shown a rectangle with dimensions $dx$ and $dy$ deformed by the displacement vector $\mathbf{u} = u_x\hat{\mathbf{x}} + u_y\hat{\mathbf{y}}$.

The normal strain in the direction $x$ is simply the relative change in the distances of the sides of the square.

$$\varepsilon_{xx} = \frac{\overline{a'b'} - \overline{ab}}{\overline{ab}} \tag{23}$$

From Fig 25 it follows directly from Pythagoras theorem:

$$\overline{a'b'} = \sqrt{\left(dx + \frac{\partial u_x}{\partial x}dx\right)^2 + \left(\frac{\partial u_y}{\partial x}dx\right)^2} \tag{24}$$

Therefore, for infinitesimal $dx$ and linear terms of the derivatives of the displacements:

$$\varepsilon_{xx} = \frac{\partial u_x}{\partial x} \tag{25}$$

And, likewise, the normal stress in the $y$ or $z$ directions (not shown, but easily generalized to three dimensions) can be defined.

Next, the engineering shear strain[11] $\gamma_{xy}$ is calculated, $\gamma_{xy} = \alpha + \beta$. Its relationship with the strain tensor is simply as $\varepsilon_{xy} = \gamma_{xy}/2$.

From Fig 25 if follows that:

---

[11] The engineering shear strain $\gamma_{xy}$ is calculated from the change in angle from the lines $\overline{ab}$ and $\overline{ac}$ to the lines $\overline{a'b'}$ and $\overline{a'c'}$, respectively. The tensorial shear strain $\varepsilon_{xy}$ is half the shear strain because in this way the equations are symmetric and are tensorial correct; the tensorial strain $\boldsymbol{\varepsilon}$ transform as a tensorial equation, but the engineering strain $\boldsymbol{\gamma}$ does not.

$$\tan\alpha = \frac{\frac{\partial u_y}{\partial x}dx}{dx + \frac{\partial u_x}{\partial x}dx} \approx \frac{\partial u_y}{\partial x} \tag{26}$$

And similarly for $\beta$. Since $dx$ is infinitesimal so does $\alpha$, therefore $\alpha \approx \tan\alpha$, and it follows that:

$$\varepsilon_{xy} = \frac{1}{2}\left(\frac{\partial u_x}{\partial y} + \frac{\partial u_y}{\partial x}\right) \tag{27}$$

Combining the formula for the normal stress (25) and shear stress (27), it follows that the stress as a function of the displacements is given by:

$$\varepsilon_{ij} = \frac{1}{2}\left(\frac{\partial u_i}{\partial j} + \frac{\partial u_j}{\partial i}\right) \tag{28}$$

Where $i, j$ are the $x, y, z$ axis.

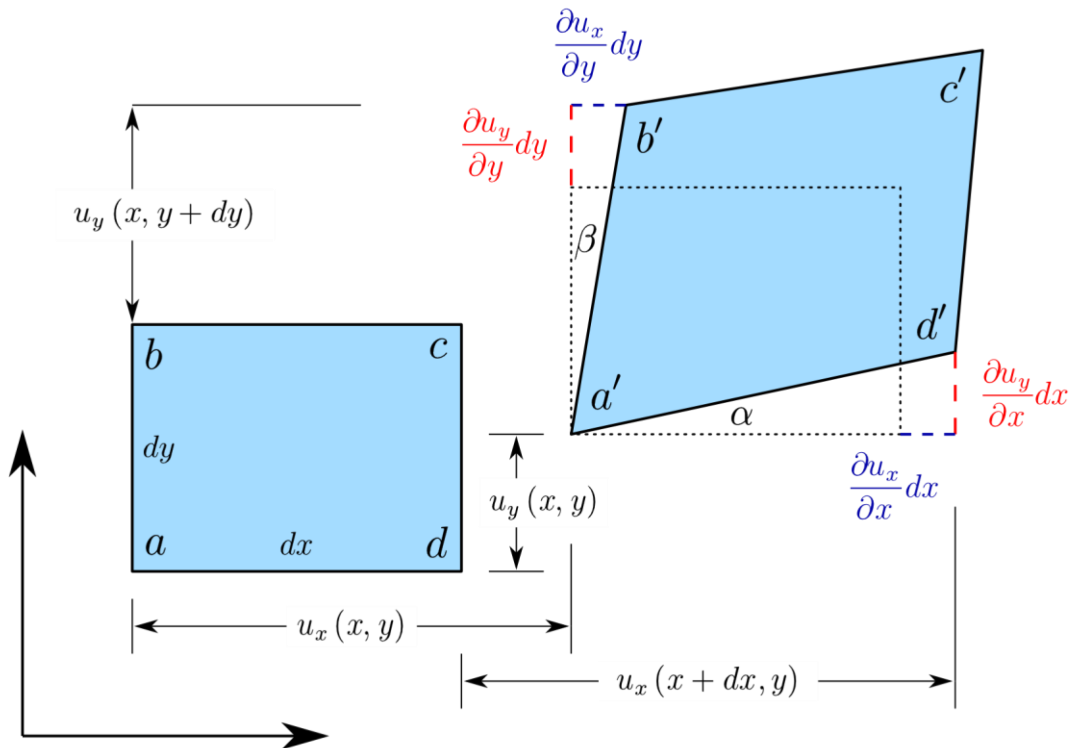


***Fig 25***. *Infinitesimal deformation.*

## Appendix B – Anisotropic cantilever

If instead of an isotropic material, as it were used in the 3D simulation (section 2.4.3 – 3D Simulation), an anisotropic material were used, what would change in the analytical theory?

To answer this question a simulation were made using the same geometry but instead of a isotropic material specified by the Young modulus, it were used an anisotropic material specified the Elasticity Matrix, a 21 parameters matrix that is used to express Hooke's law, a tensorial equation, into a matrix equation. In this way the material is still linear, but behaves differently in when loads are applied in different directions. A crystal is an example of such material. And since the cantilever is usually made of silicon or silicon nitride, using anisotropic material we are simulating a more realistic cantilever. Fig 26 shows the different materials a cantilever can be made. The cantilever is anisotropic and non-homogenous.

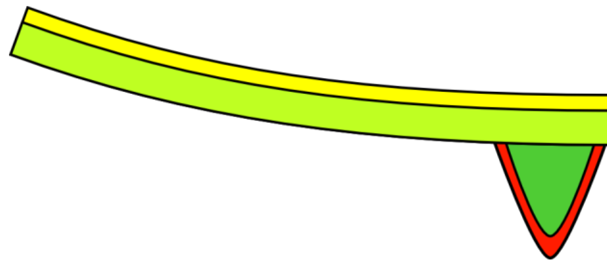

***Fig 26****. Schematic of typical materials (layers) used in the manufacture of a probe. In yellow there is the reflective coating (usually gold); in light green the body of the cantilever, made of a crystal or a polycrystal; in dark green the tip, also a crystal or polycrystal, its material can differ from the cantilever body; in red there is the tip coating.*

The elasticity matrix is material dependent, and for some materials a lot of elements are zero. To simulate the worst case scenario, a random elasticity matrix were generated, with random elements from $30GPa$ to $200GPa$. The spring constant is calculated from the inclination of the curve $u_z$ and $F_z$ with the others forces absence. Using this spring constant the graph of Fig 21 is repeated using the same analytical formulas given by in Table 1. The result is shown in Fig 27. As can be seen, the same behavior of the neutral axis is observed, with a little bit less regularity. Also the stress distribution becomes wobbly and are no-uniform, unlike the isotropic case.

So, although the description of an isotropic and anisotropic cantilever are different, in the limit of forces used (linear limit) they have the same behavior. While in the anisotropic

case is needed to specify the elasticity matrix, in the isotropic case only the Young modulus is needed, and this Young modulus, is a "mean" of the elasticity matrix, in a sense that it gives the same displacement. In others words, this mean Young modulus is related with the spring constant defined above, and the cantilever behavior is dictated by the spring constant. So this mean, or effective Young modulus can give the same behavior as the full model.

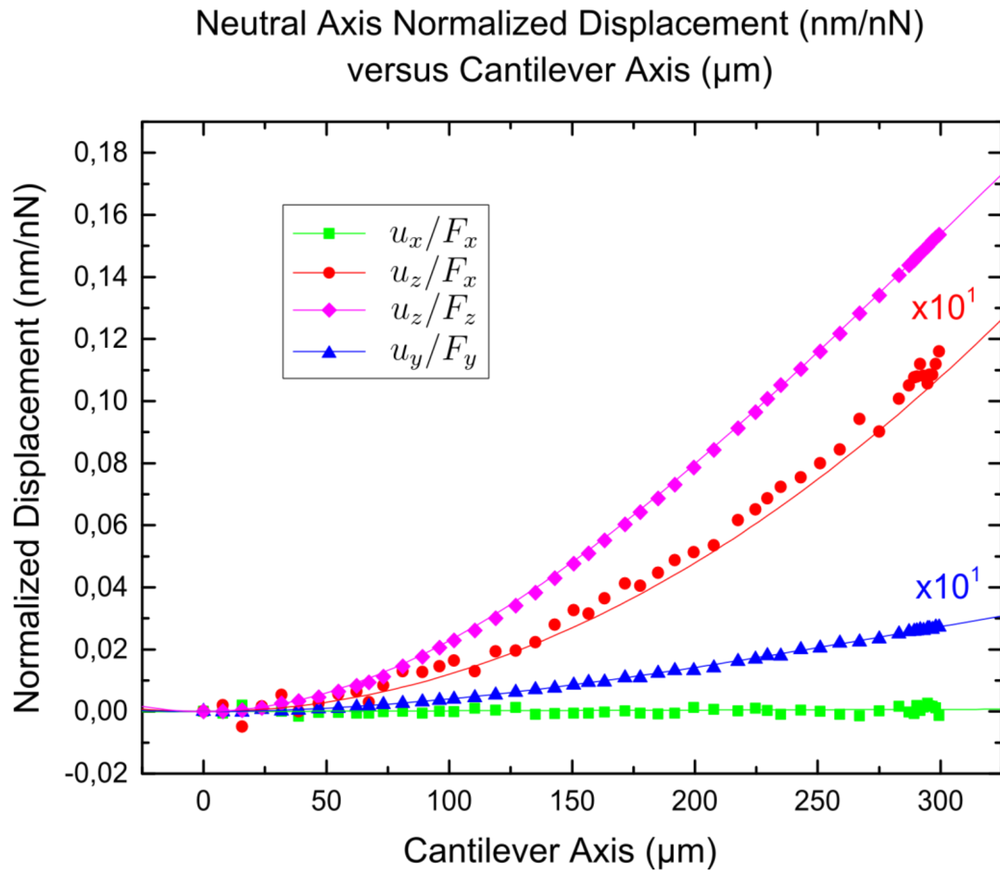


***Fig 27***. *Neutral axis normalized displacement (displacement divided by force) in function of the length along the cantilever. A dot consists of the numeric data while a solid line is the respective analytical formula plotted. Green curve consists of the normalized displacement* $u_x$ *for the force* $F_x$*; blue curve consists of the normalized displacement* $u_y$ *for the force* $F_y$ *for the bending case; red curve consist of the normalized displacement* $u_z$ *for the force* $F_x$*; magenta curve consists of the normalized displacement* $u_z$ *for the force* $F_z$*. Analytical formulas used are given in Table 1.*

## Appendix C – Compression of a cantilever

The force $F_x$ can compress the cantilever along its axis. This compression can be expressed mathematically as a displacement **u** only in the axis $x$. So we can write:

$$u_x = U(x) \tag{29}$$

Using the same reasoning as section 2.3.1 – Euler-Bernoulli Beam Theory, finding the strain $\varepsilon$ and them using Hookes law to find the stresses we get:

$$\sigma_{xx} = E\varepsilon_{xx} = E\,U'(x) \tag{30}$$

Integrating the stress (30) over the cantilever area we have the internal forces on the cantilever, equating this to the external forces (in this case $F_x$) we have:

$$\int \sigma_{xx} dA = EU'(x) \int dA = F_x \tag{31}$$

Were the area integral in (31) is $dA = dydz$, so $U'(x)$ can come out the integral. Solving this differential equation with initial conditions $U(0) = 0$ we have:

$$U(x) = \frac{x}{AE} F_x \tag{32}$$